Ore Geology Reviews 163 (2023) 105794

Contents lists available at ScienceDirect

Ore Geology Reviews

journal homepage: www.elsevier.com/locate/oregeorev

In situ trace elements and sulfur isotope analyses of layered sphalerite as a record of ore-forming processes in the world-class Jinding sediment-hosted Zn-Pb Ore Deposit, China

Lan Mu [a,b], Ruizhong Hu [b,c,*], Xianwu Bi [b], Tingguang Lan [b], Yongyong Tang [b], Youwei Chen [b], Wei Gao [b]

[a] Yunnan Minzu University, Kunmig 650504, China
[b] State Key Laboratory of Ore Deposit Geochemistry, Institute of Geochemistry, Chinese Academy of Sciences, Guiyang 550081, China
[c] College of Earth and Planetary Sciences, University of Chinese Academy of Sciences, Beijing 100049, China

ARTICLE INFO

Keywords:
Critical metals
Jinding Zn-Pb deposit
Trace elements
Sulfur isotope
LA-ICP-MS mapping
Sanjiang Tethys region

ABSTRACT

The Jinding deposit is well-known to contain high concentrations of metals Zn, Pb, Cd, Tl, Ag, etc. in the world. The associated critical metals and their substitution mechanisms were wildly concerned. This study investigated and compared sphalerites using a combination of textural, trace element, and sulfur isotopic analyses to give insights into element substitution mechanisms and possible sources of ore-forming fluids and to constrain processes involved in ore genesis of the world-class Jinding sediment-hosted Zn-Pb deposit. LA-ICP-MS analyses reveal chemical zoning in the sphalerites together with the coupling of two main groups of trace elements substitution mechanisms: one is Fe + Ge + Mn + Pb + As + Tl and vacancies to substitute Zn, and the other is Cd + Cu + Ag + Sb to substitute Zn. The incorporation of trace elements is facilitated by the replacement of Zn by Cd and Fe. These two group elements have distinct color oscillatory zonation and are intertwined in the trace element LA-ICP-MS element maps. The sulfur isotopic values show high isotope fractionation in the sphalerite from −28.4 to −0.5 ‰, suggesting a bacteriogenic sulfur origin at Jinding. Sphalerite sample has observed that sulfur isotope is correlated with Fe concentration and anti-correlated with Cd concentration. These variations in isotope fractionation and trace element disequilibrium partitioning were interpreted as the effects of temperature and pH with less influence from sulfur activity. These variability zones of sphalerite alternately enriched in Cd- and Fe-related elements suggested that ore fluids may flow from metal-fertile sedimentary/basement sequences during their ascent, and colloform sphalerite was likely formed by a high degree of supercooling, over-saturation, and rapid mixing between bacteriogenic sulfur and metal-rich in spaces of collapse dome. Based on our observations, we suggested that these variability zones of layered sphalerite alternately enriched in Cd and Fe would likely provide useful insight for a potential economic Zn-Pb and associated critical metals mineral exploration deposit.

1. Introduction

Worldwide demand for the metals Ge, Ga, Cd, In, and Tl has increased in recent years. Sphalerite is the chief ore of zinc in sulfide-rich base metal deposits, with simple formula but incorporates a broad range of trace elements such as Ga, Ge, In, Ag, Cd, Mn, Hg, As, Tl, etc. These elements can be mainly extracted from zinc ore, and sphalerite are by far the most important economic sources of Ge, Cd, In, and Tl, and Ga are second only to bauxite ores (Cook et al., 2009). Colloform textures have been described from many of the world's sulfide ore deposits (Roedder, 1968; Kuhlemann et al., 2001; Peevler et al., 2003; Di Benedetto, 2005; Barrie et al., 2009; Pfaff et al., 2011; Gagnevin et al., 2014), and commonly occur as primary depositional structures like 'framboidal' or 'colloform' textures that are cryptocrystalline to fibrous and show a banded structure. The colloform texture was thought to result from the precipitation of successive layers of microscopic euhedral crystals projecting into ore fluid (Roedder, 1968). Most researchers suggest that fluid mixing may be the most common means by which the

* Corresponding author at: State Key Laboratory of Ore Deposit Geochemistry, Institute of Geochemistry, Chinese Academy of Sciences, Guiyang 550081, China.
E-mail address: huruizhong@vip.gyig.ac.cn (R. Hu).

https://doi.org/10.1016/j.oregeorev.2023.105794
Received 31 July 2023; Received in revised form 15 November 2023; Accepted 17 November 2023
Available online 23 November 2023

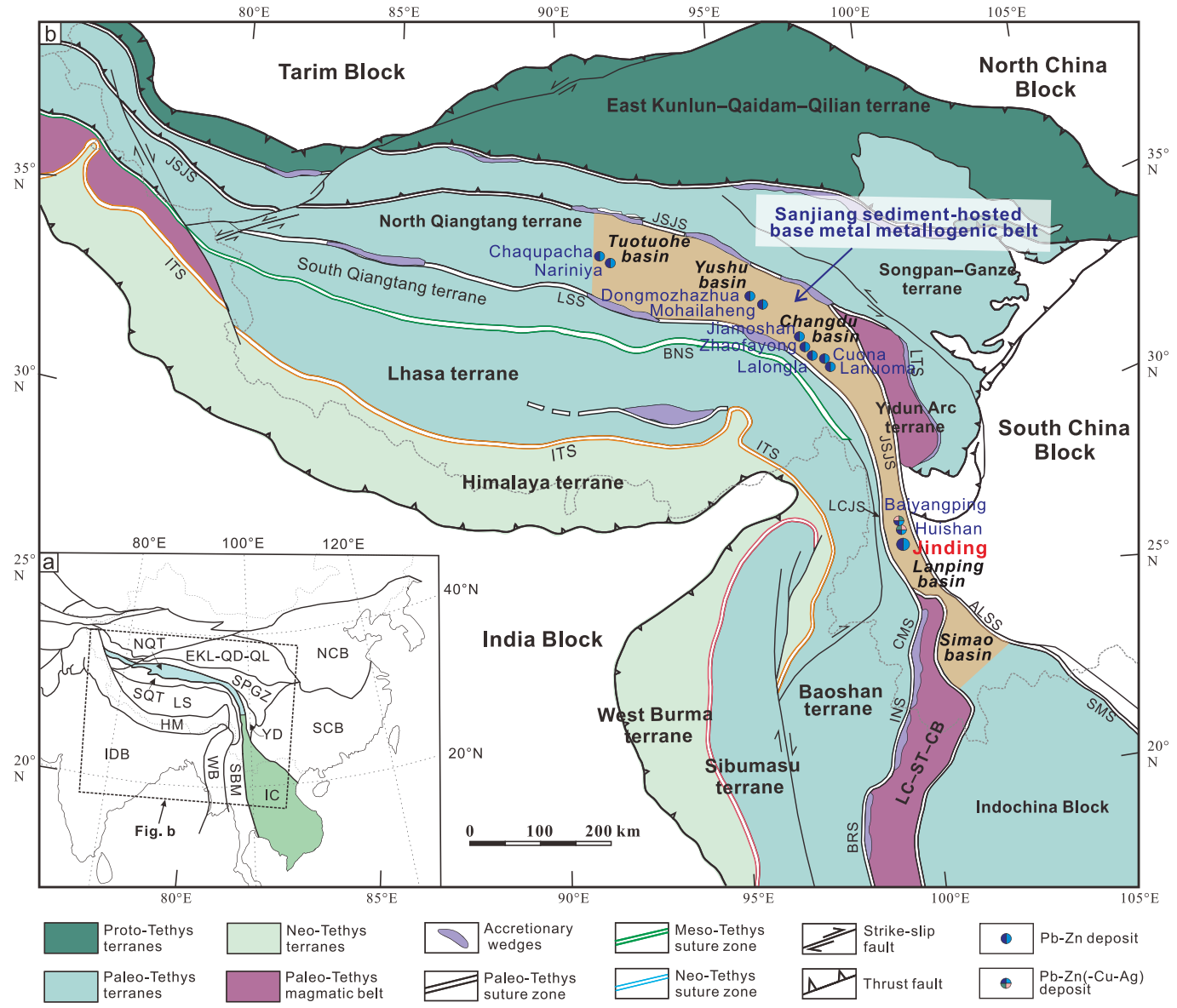

Fig. 1. (a) A simplified map of East Asia showing the distribution of the principal continental blocks and sutures (modified after Yin and Harrison, 2000). (b) Tectonic framework of the Tibetan plateau and showing the major tectonic units, structure traces, and the distribution of key sediment-hosted metal deposits within the Sanjiang sediment-hosted base metal metallogenic belt (modified from Xue et al., 2015; Li et al. 2018; Bi et al. 2019). BNS: Bangonghu-Nujiang Suture; JSJS-ALSS-SMS: Jinshajiang - Ailaoshan - SongMa Suture; LSS-LCJS-CMS-INS-BRS: LongmuTso Shuanghu - Lancangjiang - Changning Menglian - Inthanon - Burma Suture;

supersaturation required for colloform texture is achieved in nature (Paradis et al., 2007; Gagnevin et al., 2014). Therefore, the primary banded textures and preserved trace elements contain some information on the conditions of formation that potentially elucidate the sequential behavior and processes of the hydrothermal system (Barrie et al., 2009; Gagnevin et al., 2014). Importantly, some complex growth histories and element substitution mechanisms of colloform sphalerite are expected to display by the repeated sulfur and chemical variability in the composition of the mineralizing fluid.

The Sanjiang region is located on the eastern margin of the Tibetan plateau and host to several significant epigenetic sediment-hosted ore deposits (Fig. 1), which contain economically important resources of Zn, Pb, Cu, Ag, and dispersed metals such as Ga, Ge, Tl, and Cd in China (e.g., Jinding and Huoshaoyun world-class deposits). The Jinding orebody (Fig. 2) is the fourth largest Zn deposit in Asia that reserves together amount to about 220 million tonnes (Mt) at an average grade of ~ 6.1 % zinc and ~1.3 % lead (Leach et al., 2005; Third Geological Team, 1984). The element concentrations of Cd, Tl, Ag, S, and Sr are sufficiently high that can be economically exploited as a by-product. Zn-Pb mineralization at Jinding is mainly hosted by sandstone and breccias and is characterized by fine-grained disseminated and colloform ores, low-temperature mineralization (79°–173 °C; Mu et al., 2021), and a geochemical association with organic matter (Chi et al., 2017; Leach et al., 2017; Song et al., 2020). A substantial amount of research including new fieldwork, isotope analysis, and fluid inclusion studies has been carried out on the Jinding deposit and has contributed to interpretations of the genesis of the Jinding deposit (Hu et al., 1998; Kyle and Li, 2002; Chi et al., 2007, 2017; Xue et al., 2007; Tang et al., 2014; Leach et al., 2017; Mu et al., 2021). Some researchers have proposed that the deposit formed in a former hydrocarbon reservoir, and sulfide precipitation occurred by a mixture of resident reduced sulfur-bearing oil with external metal-rich hydrothermal fluids. However, given the complex textures of ore and gangue minerals and long-lived fluid activity in the Jinding deposit, the formation models of sulfides are still poorly understood and the mechanism and process of Pb-Zn mineralization have not reached a consensus yet. In addition, there is inadequate

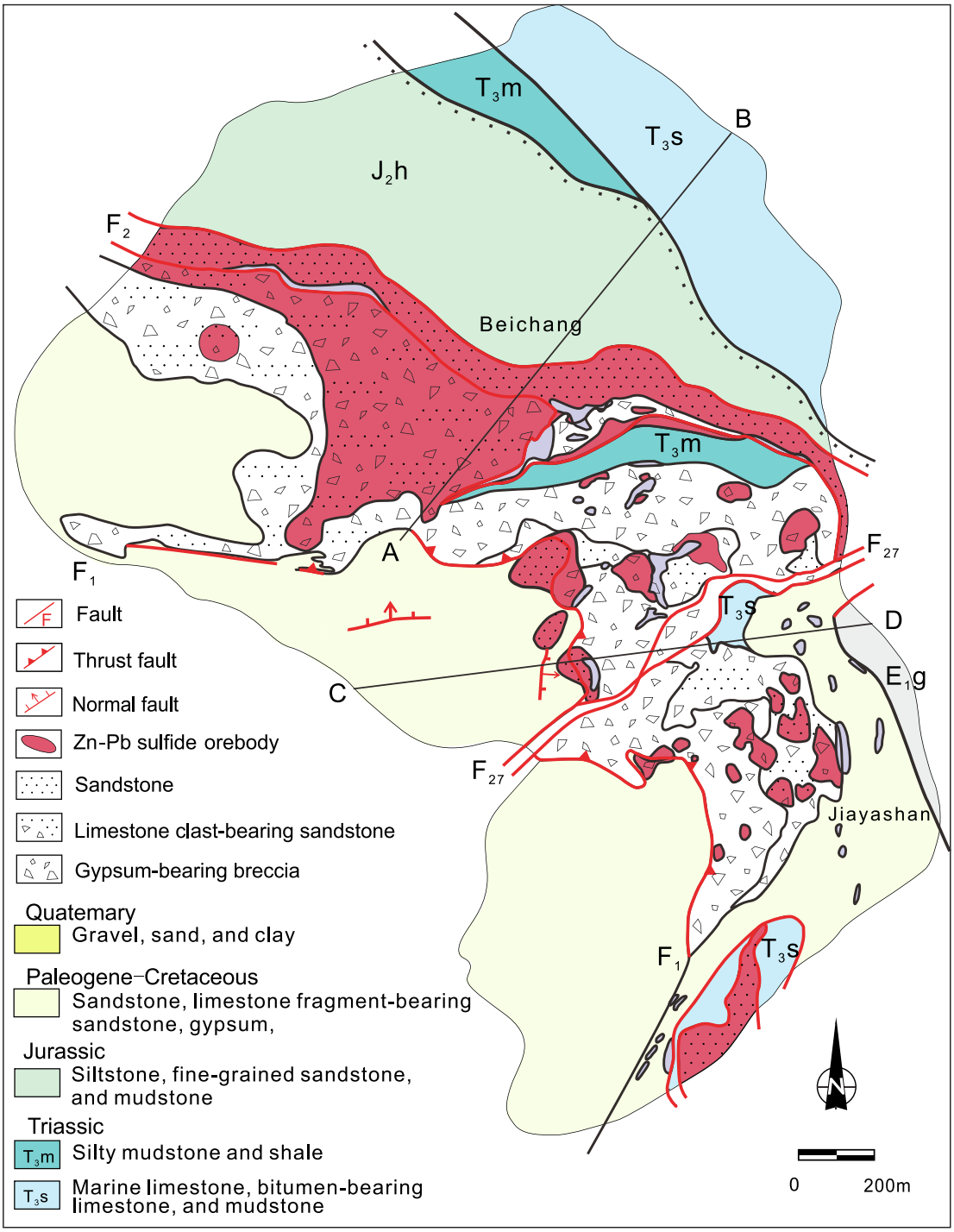

Fig. 2. Geologic map of the Jinding Zn-Pb deposit showing the geology and showing the orebody distribution in the Jinding dome (modified after Song et al., 2020). A-B and C-D indicate the locations of the cross sections in Fig. 3.

research, though, on the study of formation mechanism of colloform sphalerite, the presence of trace elements, and their substitution mechanisms.

Consequently, this study focuses on the chemical composition of sphalerite at the millimeter scale, and on the mechanism of trace and minor element incorporation during precipitation of sphalerite. We use Laser Ablation-Inductively Coupled Plasma Mass Spectrometer (LA-ICPMS) techniques to study the geochemical composition of specific zoned minerals, which provide an opportunity not only to determine concentrations at detection limits lower and high-resolution, but also provide direct or indirect information on whether a given trace element is present within the sulfide matrix or as micro- or submicroscopic inclusions of a different mineral. Moreover, we conduct in situ sulfur isotope analysis of sulfides on samples already analyzed for trace elements to assess putative sources in the sulfide. Combining the abundance of trace elements, sulfur isotopes, and field observations enables us to examine microscopic variations of geochemistry compositions in the processes of mineralization and formation models of colloform sulfide in the Jinding deposits.

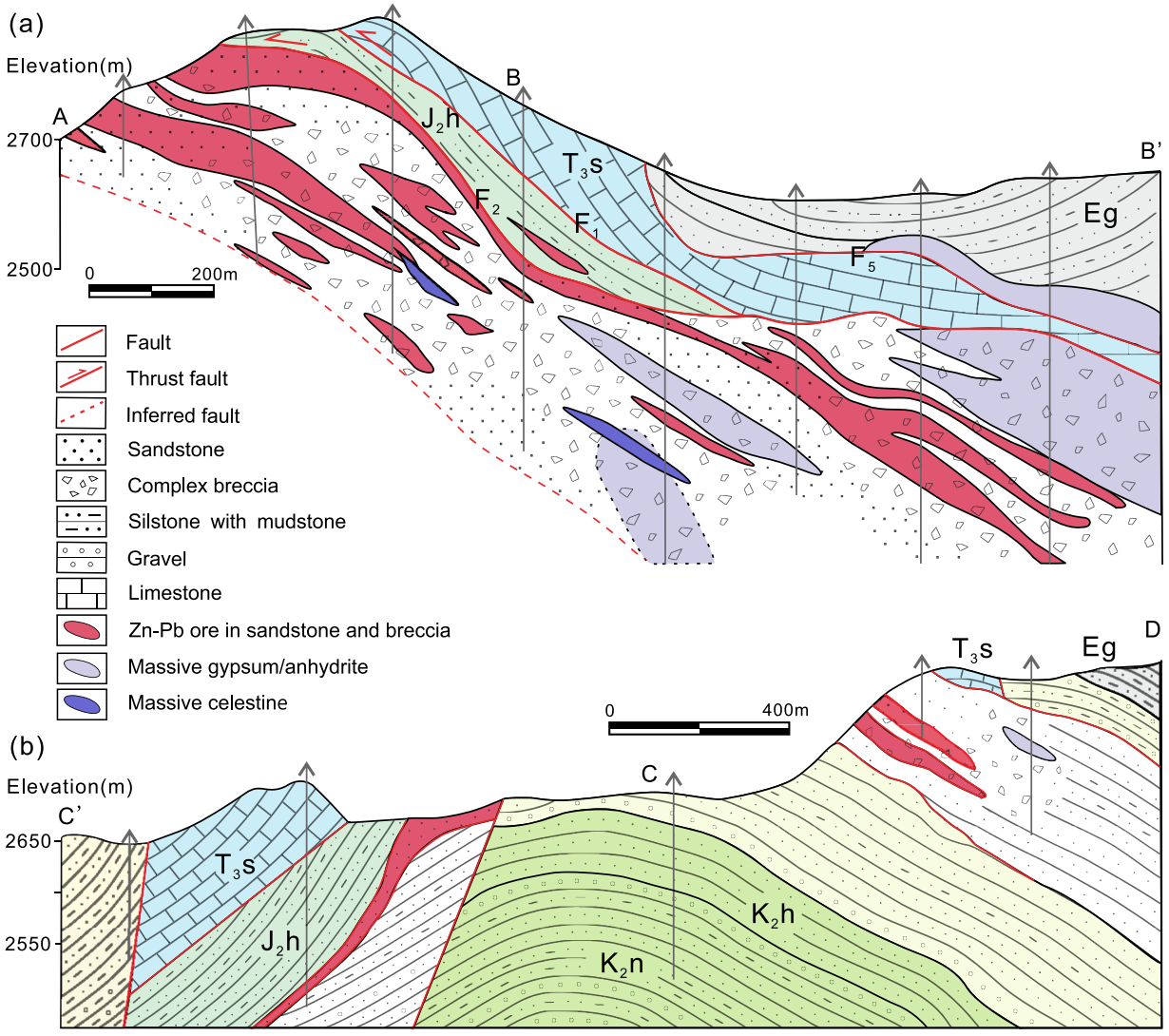

Fig. 3. Geological profiles of the Jinding Zn-Pb ore blocks: (a) SW-trending profile cross-section A-B in the Beichang-Paomaping ore block and (b) SE-trending profile C-D in the Jiayashan ore block (modified after Xue et al., 2007; Tang et al., 2014). Profile locations are shown in Fig. 2b.

2. Regional geology

2.1. Tectonic setting

The Sanjiang Tethys orogen belt extends for 2000 km along the northeastern margin of the Tibetan plateau from the Qinhai in the northwest to the Yunnan in the southwest (Fig. 1). It constitutes a collage of the Gondwana-derived microcontinental blocks, arc terranes, sub-parallel sutures, and Mesozoic basins between the sutures (Mo et al., 1994; Metcalfe, 2002; Deng et al., 2014b). After the closure of the Paleo-Tethys Oceans in Permo-Triassic, the Sanjiang orogenic belt records a complex, multistage orogenic history involving Meso- and Neo-Tethyan oceanic subduction from late-Permian to Paleocene and Indo-Asian continental collision from Paleozoic to Cenozoic (Mo et al., 1994; Metcalfe, 2002, 2013; Yin and Harrison, 2000, Deng et al., 2014b; Wang et al., 2014). The Cenozoic tectonics of Sanjiang is characterized by several large-scale strike-slip ductile shear zones including the Ailaoshan-Red River, Chongshan, and Gaoligongshan from east to west, and intense deformation of the crusts including the geometric shape distortion, the crustal thickness, and large-scale fault (Tapponnier et al., 1990; Chung et al., 1997; Spurlin et al., 2005; Deng et al., 2014b). The geological processes in the Sanjiang were thought to be dominantly controlled by the movements of surrounding larger blocks, i.e., the Indian continent, South China block, and Kunlun-Qaidam block (Fig. 1b, Deng et al., 2014b). The post-India Eurasia continental collisional extrusion tectonics induced lithosphere shortening, continental arc magmatism, and underthrusting of the South China plate resulting in the kinking of Sanjiang, expressed by block rotation, extrusion, and shearing in the southern Sanjiang, which come with numerous ore deposits of diverse genetic types and metal speciations, including porphyry-skarn Cu-(Au-Mo), Mississippi valley type (MVT) Pb–Zn, and orogenic Au (Fig. 1b, Chung et al., 1997, 1998; Hou et al., 2007; Deng et al., 2014a; Yang et al., 2020).

The Lanping Basin, developed in the northern Lanping-Simao block of the Sanjiang Tethys domain, formed from rifting and post-collisional extension during the Late Triassic (Fig. 1, Tao et al., 2002; Pan et al., 2003). The Lanping-Simao block is separated from the Yangtze Platform to the east by the Ailaoshan-Red River shear zone, and from the Tengchong and Baoshan blocks to the west by the Chongshan–Biluoxueshan shear zone, respectively. The block is covered by Triassic to Paleogene sedimentary formations with some Triassic volcanic rocks. Triassic bimodal arc volcanic rocks and volcano-sedimentary sequences are exposed along the margin of the block (Mo et al., 1994; Wang et al., 2001; Yang et al., 2014). In the Late Triassic, the Lanping Basin was filled by Triassic marine limestones, clastic rocks, and sandy mudstones, which is thought to be a post-collisional rift basin (Third Geological

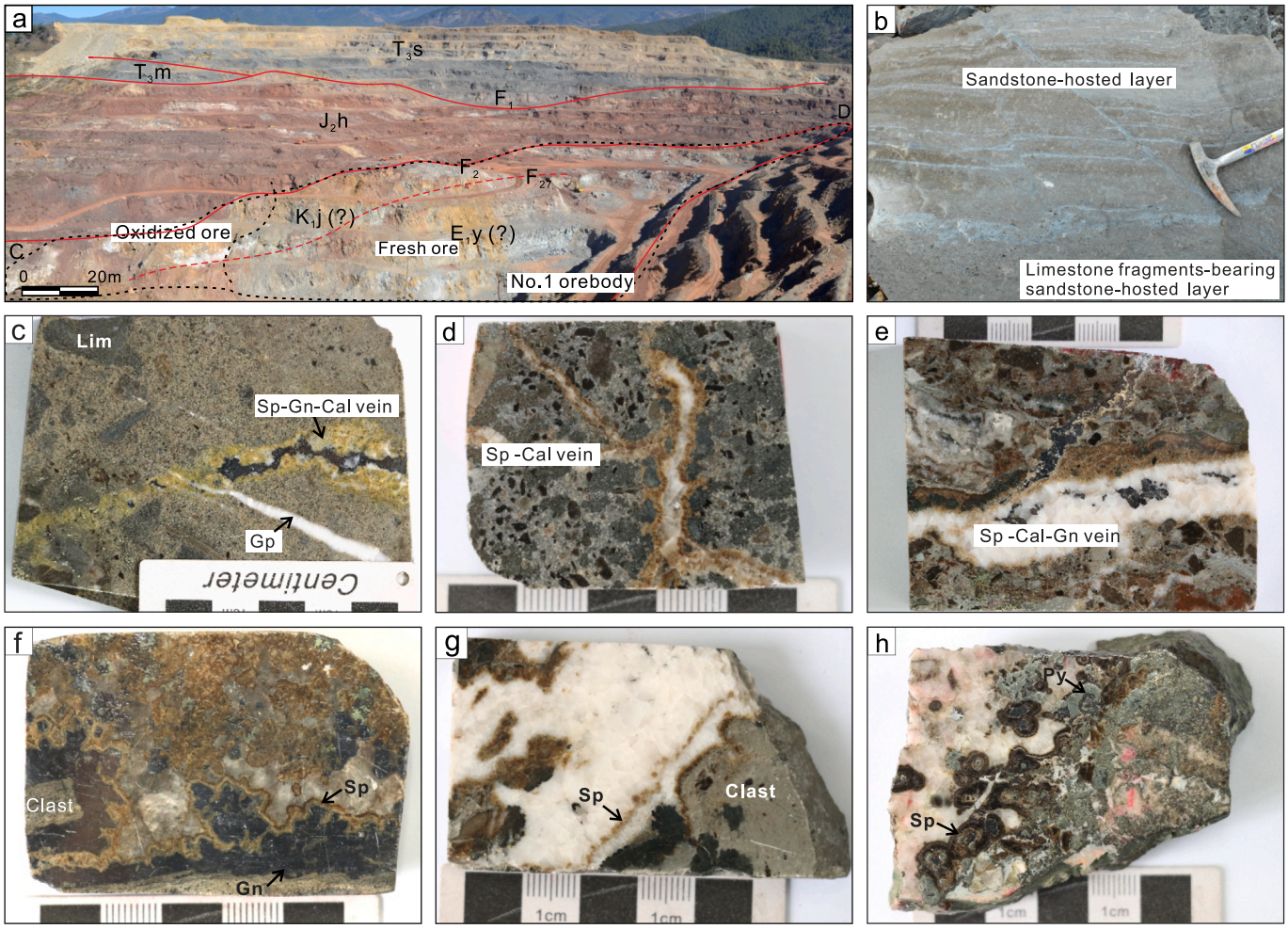

Fig. 4. Field and hand-specimen photos of typical Zn-Pb ores from Jinding. (a) SE-NW trending section photo of the Beichang open pit; (b) Disseminated ore in sandstone and limestone-fragments-bearing sandstone layers, the light gray veins are more enriched sulfide than the surrounding; (c) Sulfide veins in the early disseminated sandstone ore, with gypsum vein intruded after sphalerite-galena-calcite vein; (d) Sphalerite-calcite veins in the early limestone-lithic sandstone ore; (e) Galena-calcite veins intruded after sphalerite-galena-calcite vein in the early limestone-lithic sandstone ore; (f) Colloform Sp2 are overgrown or enveloped the galena; (g-h) Sphalerite fill in open spaces of breccia clasts. Cal = calcite, Ga = galena, Gp = gypsum, Lim = limestone breccias, Py = pyrite, Sp = sphalerite.

Team, 1984; Tao et al., 2002; Pan et al., 2003). The Jurassic and Cretaceous were largely filled by terrestrial red beds with minor carbonates, and the Cenozoic was controlled by the India-Asia collision where terrestrial clastic rocks including mudstone, sandstone, and conglomerate were deposited (Yunnan Bureau Geological Mineral Resource, 1990). Since the continental collision, the Lanping Basin Mesozoic sequences were NE–SW shortened strongly folded and thrust into nappes (Mo et al., 1994; Yin and Harrison, 2000; He et al., 2009). Extrusion or rotation of blocks around Sanjiang led to large-scale sinistral strike-slip shearing in the Chong Shan and Ailao Shan shear zones and N–S-trending strike-slip faulting in the central part of the Lanping and Simao basins (Fig. 1b; Tapponnier et al., 1990; Liu et al., 2004, 2012; Spurlin et al., 2005; Zhang et al., 2010; Yang et al., 2014).

Evaporites around the Lanping Basin occur in the Late Triassic carbonate sequences, the Middle Jurassic red beds, and the Paleocene red beds with a thickness varying from ~10 to ~500 m (Third Geological Team, 1984). The evaporites are dominated by gypsum and anhydrite and some contain abundant halite. The developments of large-scale evaporites and terrestrial red beds indicate a long-term arid environment in the Lanping basin, especially during the early Paleogene when thick evaporites were deposited (Yunnan Bureau Geological Mineral Resource, 1990; Gao, 1991).

2.2. Deposit geology

The Jinding Zn-Pb deposit is located in a tectonic dome of the northern Lanping basin, adjacent to the NNE-trending Bijiang fault which belongs to a secondary fault of the regional Lanping-Simao system (Fig. 1; Chi et al., 2006, Chi et al., 2007). The Jinding dome is defined as a structural slice related to a thrust fault to the east and the diapiric migration of Late Triassic evaporites (Leach et al., 2017; Song et al., 2020). The upper part of the dome is an allochthonous thrust slice including an inverted sequence of Late Triassic Maichuqing (T3m), Sanhedong (T3s), and Waigucun (T3w) Formations carbonate and mudstone and Middle Jurassic Huakaizuo (J2h) Formation siltstone, mudstone, and sandstone (Fig. 2).

The lower part of the Jinding deposit is separated by a thrust fault (F2) from the upper dome and was regarded as an autochthonous succession. Almost all the Jinding ores are hosted in these lower part rocks, distributed around the core of the tectonic dome and along with interlayered fracture zones (Figs. 2, 3). The host rocks are a suite of sandstones, limestone fragment-bearing sandstones, and complex breccias that used to be classified as the Late Cretaceous Jingxing (K1j) and the Paleocene Yunlong (E1y) Formations (Third Geological Team, 1984) and are now interpreted to be a mixed, sediment-evaporite mélange during regional compression thrust the hanging-wall Triassic-Jurassic rocks (Leach et al., 2017; Song et al., 2020). More than 100 orebodies

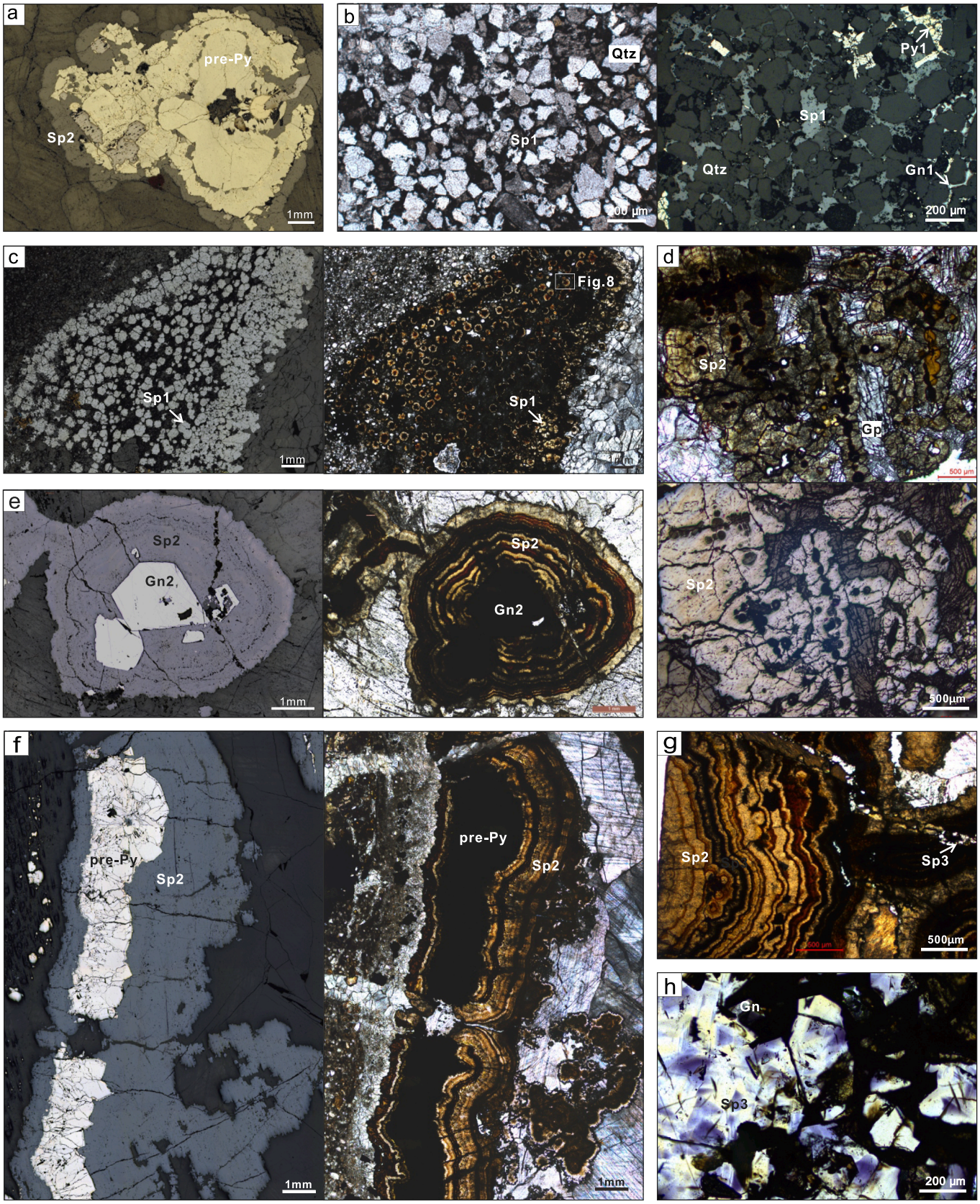

Fig. 5. Thin-section photomicrographs (reflected light and transmitted light) of typical Zn-Pb ores from Jinding. (a) Pre-ore pyrite grain has microspheres inside and were overgrown by colloform Sp2; (b) Disseminated sphalerite, galena, and pyrite/marcasite replace the carbonate in sandstone; (c) Fine-grained sphalerite replace the carbonate in sandstone; (d) Concentric sphalerite in the pre-ore gypsum; (e) Colloform sphalerite are overgrown or enveloped the galena; (f) Colloform sphalerite are overgrown the pyrite; (g) Colloform sphalerite is crosscut by crystalline sphalerite vein; (h) Coarsely crystalline sphalerite (Sp3) associated with galena in open spaces of breccia.

Table 1
Detailed information of the samples collected for analysis from the Jinding deposit.

Location	Blocks and elevation (asl/m)	Host rock	Paragenetic sequence	Sulfide type	Sample	Description
No. 1 ore body at North Jinding	BC, 2569	Sandstone	Early ore-stage	Sp1	JDBC8-2	Disseminated sphalerite with bits of galena, and pyrite
	BC, 2600	Sandstone	Early ore-stage	Sp1	JDBC16-2	Disseminated sphalerite with bits of galena, pre ore pyrite, and marcasite
	BC, 2580	Sandstone	Early ore-stage	Sp2	JDBC4-1b	Colloform sphalerite and calcite veins with bits of pyrite intergrown with sandstone
	BC, 2576	Breccias	Early ore-stage	Sp2	JDBC21-5-1	Colloform sphalerite intergrow with pyrite and sandstone
	BC, 2576	Breccias	Early ore-stage	Sp2	JDBC9-2-4b	Crystalline sphalerite, pyrite, coarse euhedral galena, and zoned calcite
	BC, 2576	Breccias	Early ore-stage	Sp2	JDBC22-4-5	Colloform sphalerite intergrow with pyrite and galena
	BC, 2588	Breccias	Early ore-stage	Sp2	JDBC27-2b	Colloform sphalerite intergrow with pyrite
	BC, 2588	Breccias	Ore-stage	Sp2, Sp3	JDBC22-6-4a	Colloform sphalerite and calcite veins were cut by crystalline sphalerite and calcite veins
	BC, 2567		Ore-stage	Sp2, Sp3	JDBC9-2-1	Crystalline sphalerite intergrown with colloform sphalerite, with bits of galena and pyrite
West Jinding	FZS, 2340	Sandstone	Early ore-stage	Sp1	JDFZS11-1	Disseminated galena, sphalerite and locally minor pyrite
East Jinding	PMP, 2140	Mainly LBS	Early ore-stage	Sp2	JDPMP-1-1-3	Nodular aggregate sphalerite in the gympsum

Abbreviations: asl = above sea level, FI = fluid inclusion, BC = Beichang, FZS = Fengzishan, PMP = Paomaping, LBS = limestone-bearing sandstone, Cal = calcite, Cls = celestine, Ga = galena, Gp = gypsum, Py = pyrite, Sp = sphalerite, NS = not successful due to the small size of fluid inclusions.

occur as irregular lenses, tabular and veins, and are distributed around the Jinding dome. The No. 1 orebody, extended for 1450 m along the northeast strike with an average thickness of 54 m, hosted the most of Zn-Pb ore reserve in the Jinding deposit. Beichang block in open-pit-mine and Paomaping block in underground mine are the most economic and mainly mining areas (Figs. 2, 3). Others include Jiayashan in the east, Fengzishan and Xipo in the west, Baicaoping and Nanchang in the south. The Jinding deposit has a total reserve of ~220 million tonnes (Mt) of ore with primary sulfide ores accounting for 63 % of the ores (at 5.6 % Zn + Pb). The oxidized ores account for 29 % of the total ores and generally have a higher grade at 12 % Zn + Pb (Shi et al., 1983; Third Geological Team, 1984; Qin and Zhu, 1991). The prominent F27 fault in Jinding dips steeply, varies in width, and separates the Beichang and Jiayashan ore blocks (Figs. 3, 4a). The fault serves as the boundary between the sandstone unit and the red gypsum-bearing mélange (Song et al., 2020). The petrographical evidence has proved that the deposit experienced a sequence of complex geologic events and the ore formation is affected by multiple hydrothermal events. A paleo-oil–gas reservoir accumulated at the Jinding dome before the Zn-Pb mineralization (Xue et al., 2015, Chi et al., 2017). The bitumen Re-Os dated at 68 ± 5 Ma (Gao et al., 2012) and pyrite Re-Os dated at 72.9 ± 0.5 Ma (Huang et al., 2021) are believed to be the age of oil generation. Zn-Pb mineralization has been constrained to 35.9 to 25.8 Ma by apatite fission track dating (Li et al., 2000), 23 ± 3 Ma by paleomagnetic dating (Yalikun et al., 2017).

3. Mineralogy

Primary sulfide mineralization at Jinding is hosted mainly in the disseminated sandstone and clast-bearing sandstone, highly competent and permeable breccias, and vein ores. The dominant ore type is characterized by fine-grained sulfides including sphalerite, galena, pyrite, and marcasite disseminated in sandstones and clast-bearing sandstone and has replaced the calcite cement (Fig. 4b-h). They are mostly in the upper portion of the deposit (Fig. 3). The type of breccias ore is dominated by the replacement of sulfides, calcite, gypsum, and celestine in the breccia matrix. The breccias comprise angular Late Triassic limestone, siltstone, and mudstone clasts (Gao, 1989), generally 0.1 to 5 cm in diameter and some reach up to 3 m (Fig. 4d). Sulfides fill in open spaces of matrix and breccia clasts (Fig. 4f-h). Gypsum/anhydrite is abundant in the Jinding breccia zone and commonly has a flow texture that is interpreted to be the migration of the breccia clasts and matrix evaporite in diapiric zones (Leach et al., 2017). Some sulfide minerals occur as veinlets with a variety of crosscutting relationships and textures in the fractures in sandstones and breccias (Fig. 4b-d). Minerals in the study area include pyrite, marcasite (as a polymorph of FeS_2, pyrite is used to represent the mixed pyrite-marcasite in this paper), sphalerite, galena, calcite, anhydrite, gypsum, celestine, barite (as a barite-celestine solid solution, celestine is used to represent the mixed barite-celestine in this paper), and bitumen (Figs. 4, 5). On the basis of the morphology, overgrowth relationships, and paragenesis, four stages of sulfides are interpreted to have grown: syngenetic or diagenetic pre-ore stage; hydrothermal early ore-stage associated with disseminated and colloform sulfides in sandstone and breccias; late ore-stage associated with coarse-grained sulfides in breccias; and post ore stage without mineralization (Table 1).

The earliest-formed minerals in the pre-ore stage of the Jinding deposit are pre-ore calcite and celestine, gypsum, and anhydrite and some subsequently have been replaced by pyrite as a result of the accumulation of reduced S in the paleo-oil–gas reservoir. The pre-ore pyrite and calcite are pervasive in Jinding and are more abundant than the ore stage pyrite and calcite. The grains have distinct growth bands and sometimes contain organic matter impurities, mainly within microspheres inside the pyrite grains (Fig. 5a). The pre-Py samples are considered to occur as two types: organic matter-free (that yields a Re-Os isochron age of 51 ± 1 Ma) and organic matter-bearing (yield a Re-Os isochron age of 72.9 ± 0.5 Ma, Huang et al., 2021).

The ore stage in the Jinding deposit is divided into the early ore stage and the late ore stage (Mu et al., 2021). The early ore stage is characterized by cement-related sulfides. In sandstone and limestone fragments-bearing sandstone, they mainly consist of abundant fine-grained hydrothermal sulfides including sphalerite (ore-Sp1), galena (ore-Gn1), and pyrite (ore-Py1) (Fig. 4b-d). Disseminated Sp1 was the most abundant sphalerite type precipitated in Jinding deposit. The sulfides mainly occur as disseminations in the sandstones and cemented the detrital quartz grains (Fig. 5b, c). These sulfides are anhedral to fine-grained and between 20 and 500 μm in diameter (Fig. 5b, c). Sp1 is characterized by porous cores of flaws or inclusions. The colloform and microcrystalline sphalerite (Sp2), galena (Gn2), and pyrite (Py2) that occur in fractures of sandstones and breccias are also belonged to the early-stage (Fig. 4c, d). Colloform sphalerite has concentric zoning that different bands parallel to the same growing face. In breccias, colloform Sp2 and Gn2 commonly surround fragments of sandstone or limestone and replaced the pre-ore calcite and gypsum (Fig. 4e, 5d). In some cases,

Table 2
Summary of LA-ICP-MS Analyses of trace element concentrations of sphalerite from the Jinding deposit.

	Ti ppm	Mn ppm	Fe ppm	Co ppm	Cu ppm	Ga ppm	Ge ppm	As ppm	Mo ppm	Ag ppm	Cd ppm	Sb ppm	Hg ppm	Tl ppm	Pb ppm
Sp1 JDBC8-2 *(n=12)*															
Min	10.7	0.2	35.7	0.1	37.5	0.1	0.1	0.4	0.0	2.1	3870	0.2	1.7	0.2	8.9
Max	42.4	8.4	283	1.0	951	16.2	23.6	41.0	8.2	49.0	9215	37.1	4.6	3.5	420
Average	14.5	3.3	109	0.7	381	4.0	5.6	9.0	1.6	22.5	6052	10.8	3.0	1.6	168
SD	8.5	2.7	67.2	0.3	262	4.5	7.6	12.2	2.5	18.7	1532	10.9	0.9	1.0	137
JDBC16-2 *(n=10)*															
Min	9.5	5.0	147	BDL	0.4	6.7	1.3	0.4	0.1	0.3	675	0.0	1.8	0.4	7.2
Max	19.5	67.3	908	BDL	1.9	22.8	61.3	60.3	1.8	0.6	5110	4.3	6.5	19.0	104
Average	12.8	36.1	443	BDL	0.9	14.6	21.9	10.6	0.6	0.4	2792	1.2	3.3	5.7	58.3
SD	3.3	20.0	212	BDL	0.6	4.8	18.0	17.4	0.7	0.1	1600	1.4	1.3	5.3	32.5
JDFZS11-1 *(n=12)*															
Min	15.9	0.5	13.2	1.8	278	0.3	0.2	0.3	0.0	26.3	4879	0.8	2.8	0.4	43.9
Max	48.2	1.9	174	3.4	855	3.7	2.1	2.9	0.4	927	60,560	18.4	9.9	1.5	210
Average	20.4	1.0	44.3	2.5	522	1.2	0.8	1.4	0.1	191	35,705	7.4	6.4	1.1	123
SD	8.7	0.5	45.4	0.5	184	0.9	0.7	0.8	0.1	249	17,836	5.7	2.2	0.3	46.1
Sp2 JDBC22-6-4a *(n=16)*															
Min	3.4	3.5	89.8	0.1	1.3	0.1	0.5	0.5	0.2	1.4	4079	0.6	1.6	2.8	126
Max	6.8	127	16,107	0.3	310	1.5	83.1	1025	0.3	104	15,515	6.5	4.5	253	2112
Average	4.9	52.5	4707	0.1	74.7	0.5	21.5	274	0.2	31.5	8373	2.3	2.7	75.0	1045
SD	0.7	36.7	5341	0.1	91.8	0.4	23.4	321	0.0	32.1	3456	1.6	0.8	80.5	546
JDBC4-1b *(n=10)*															
Min	4.0	1.7	59.5	0.2	0.6	0.2	1.1	0.7	0.8	7.7	2254	0.1	1.4	0.7	82.5
Max	5.7	20.2	618	6.6	14.8	1.0	13.1	18.3	0.8	92.2	14,138	5.7	4.0	5.9	802
Average	4.7	12.0	261	1.6	5.0	0.5	4.4	6.8	0.8	49.2	7111	2.7	2.8	3.1	299
SD	0.4	5.8	205	2.1	4.2	0.2	3.4	6.9	0.0	33.8	3860	1.5	0.9	1.5	223
JDPMP-1–1-3 (n=14)															
Min	4.2	0.5	36.0	0.1	72.8	0.2	0.1	0.7	0.1	3.8	1069	0.8	1.7	1.4	91.7
Max	5.5	12.8	1223	0.7	548	3.9	12.5	505	4.3	140	21,903	77.4	41.3	66.2	2570
Average	5.0	6.3	372	0.3	298	1.7	5.9	201	1.1	59.2	7809	28.9	17.2	24.4	1033
SD	0.4	4.6	319	0.2	138	1.3	4.1	173	1.6	37.0	6057	29.3	14.6	22.1	839
JDBC21-5-1a *(n=5)*															
Min	4.0	45.7	904	0.1	0.6	1.6	10.4	29.2	7.2	0.5	173	0.1	2.2	4.3	644
Max	7.3	107	7610	1.6	0.6	15.3	110	229	7.2	2.5	674	2.8	2.5	58.4	1048
Average	5.1	71.8	3880	0.7	0.6	7.0	48.5	134	7.2	1.4	353	1.1	2.4	33.2	832
SD	1.2	22.8	2455	0.5	0.0	5.1	35.5	84.3	0.0	0.7	172	1.1	0.1	20.5	150
JDBC21-5-1a *(n=21)*															
Min	3.8	0.5	11.1	0.0	0.7	0.1	0.2	0.4	0.6	0.5	104	0.1	1.2	2.1	79.3
Max	5.7	98.8	3521	5.7	17.4	2.3	61.3	145	49.2	58.9	8750	1.9	3.8	41.3	822
Average	4.7	21.7	588	1.0	3.1	0.5	5.3	31.5	32.8	6.2	3416	0.4	2.1	7.8	354
SD	0.4	26.5	995	1.5	4.8	0.5	13.9	47.9	22.8	12.8	3157	0.5	0.8	9.4	215
JDBC9-2–1 *(n=12)*															
Min	3.8	7.4	141	0.1	0.8	0.0	0.2	0.4	BDL	0.7	1937	0.2	1.1	1.9	110
Max	6.0	108	1073	0.3	266	0.1	9.5	70.2	BDL	154	14,006	5.5	7.7	12.8	495
Average	4.8	27.7	436	0.1	73.8	0.1	2.6	10.8	BDL	54.8	8160	2.1	2.7	4.6	330
SD	0.6	28.7	325	0.1	78.6	0.0	3.5	19.9	BDL	44.5	3373	1.7	1.7	2.8	121
Sp2 JDBC22-4–5 *(n=38)*															
Min	3.6	0.6	10.5	0.1	0.4	0.1	0.2	0.5	0.1	0.3	1522	0.2	1.0	0.9	54.7
Max	6.1	300	26,572	21.2	517	2.9	233	1659	0.3	425	22,041	13.2	17.0	433	4023
Average	4.7	99.2	6069	2.3	105	0.5	37.6	462	0.1	71.1	8158	1.9	2.5	112	1495
SD	0.5	80.1	7203	6.3	136	0.6	46.3	551	0.1	93.0	4629	2.5	3.0	142	1046
JDBC27-2b *(n=15)*															
Min	11.3	0.3	37.0	BDL	0.3	0.1	0.3	0.8	0.0	0.4	49.4	0.0	0.7	0.0	0.1
Max	14.3	456	24,625	BDL	0.4	14.1	132	1391	0.1	0.7	4721	0.2	4.2	273	3984
Average	13.2	64.3	3958	BDL	0.3	2.5	25.6	235	0.1	0.5	1164	0.1	2.5	37.1	670
SD	0.8	112	6721	BDL	0.1	3.8	38.7	413	0.0	0.1	1502	0.1	0.9	73.6	1043
JDBC9-2-4b *(n=12)*															
Min	14.2	5.5	191	0.0	2.4	0.0	0.1	0.4	0.0	2.6	2601	0.4	2.3	1.1	106
Max	17.3	66.5	12,650	2.2	96.0	0.5	46.8	1006	15.9	54.5	11,737	5.6	7.1	268	1104
Average	15.5	29.1	4293	0.3	27.6	0.2	10.6	230	4.3	18.7	5787	1.9	4.1	54.9	393
SD	0.8	16.7	3863	0.6	24.4	0.2	12.3	280	5.5	17.8	2772	1.5	1.5	74.9	267
Sp3 JDBC22-6-4a *(n=10)*															
Min	4.8	0.4	77.8	BDL	2.7	0.4	0.4	0.4	BDL	1.0	8831	0.1	3.0	0.1	1.6
Max	7.0	2.0	706	BDL	41.9	27.9	28.6	0.4	BDL	11.8	13,468	0.6	6.6	0.2	17.6
Average	5.6	0.8	221	BDL	20.4	6.8	6.5	0.4	BDL	3.4	10,345	0.3	4.3	0.1	6.1
SD	0.7	0.7	197	BDL	11.8	7.5	8.1	0.0	BDL	3.0	1398	0.1	1.1	0.1	4.8
JDBC9-2-4b *(n=13)*															
Min	13.7	3.7	62.7	0.0	0.3	0.0	0.1	0.6	0.1	0.8	586	0.5	1.5	2.5	122
Max	16.4	77.6	8051	6.0	103	0.9	44.2	136	167	53.9	10,171	51.0	4.6	34.7	1040
Average	15.1	30.8	1224	1.7	25.0	0.4	7.2	32.1	24.2	14.3	4233	7.8	2.8	9.0	331
SD	0.8	22.6	2118	1.7	27.3	0.3	11.1	46.0	50.3	13.8	2533	13.5	0.8	9.1	273
Sp3 JDBC9-2–1 *(n=14)*															
Min	4.0	0.3	298	0.1	0.5	0.5	0.4	BDL	BDL	0.5	2967	0.1	2.3	BDL	0.1
Max	6.4	1.6	630	0.1	42.3	2.2	9.5	BDL	BDL	1.5	6753	0.1	4.1	BDL	3.9
Average	4.9	0.9	464	0.1	15.6	0.9	4.0	BDL	BDL	0.8	4389	0.1	3.3	BDL	1.3
SD	0.6	0.4	88.0	0.0	13.1	0.5	3.0	BDL	BDL	0.3	1036	0.0	0.5	BDL	1.2

Notes: BDL = below detection limit, the counts only contain the content > the minimum detection limits; n = number; SD = 1 standard deviation.

Table 3
Summary of LA-ICP-MS Analyses of trace element concentrations of pyrite from the Jinding deposit.

	Ti	V	Mn	Co	Ni	Cu	Zn	Ge	As	Mo	Ag	Cd	Sb	Tl	Pb
	ppm	ppm	ppm	ppm	ppm	ppm	ppm	ppm	ppm	ppm	ppm	ppm	ppm	ppm	ppm
Pre-Py JDBC16-2 *(n = 8)*															
Min	33.3	0.1	25.8	0.0	0.1	0.4	3.5	0.2	85.5	0.2	0.1	0.2	0.1	11.9	992
Max	40.5	0.2	82.9	0.1	0.6	3.1	16.9	0.7	685	3.1	1.4	0.9	4.1	50.0	18,003
Average	37.3	0.1	51.4	0.1	0.4	1.7	9.6	0.3	428	1.3	0.7	0.5	1.1	29.4	5195
SD	2.3	0.0	17.0	0.0	0.2	1.1	3.9	0.2	202	1.0	0.5	0.3	1.4	10.5	5176
Pre-Py JDBC21-5-1a *(n = 16)*															
Min	12.7	0.1	18.9	0.1	0.2	0.4	3.1	0.1	37.0	0.3	0.1	0.3	0.1	49.2	727
Max	16.2	1.0	578.2	3.2	2.5	0.4	58.3	3.5	8665	68.6	4.0	0.8	4.3	999.6	11,749
Average	14.5	0.3	185.1	0.6	0.6	0.4	16.7	0.7	1832	19.7	0.8	0.5	1.2	272.1	4833
SD	1.1	0.2	175.4	0.8	0.6	0.0	15.1	0.8	2473	21.4	1.2	0.2	1.5	300.5	3388
Pre-Py JDBC21-5-1a *(n = 19)*															
Min	11.1	0.1	27.1	0.04	0.2	0.7	5.0	0.1	1.3	0.2	0.1	0.3	0.1	37.3	1639
Max	16.6	6.0	1880	147	388	1.6	59.8	9.8	21,943	157	10.0	1.5	11.0	655	10,946
Average	13.4	1.0	487	20.0	50.0	1.1	20.0	2.5	4844	40.7	1.3	0.7	1.8	246	4705
SD	1.3	1.5	492	40.7	111	0.4	14.2	3.2	8148	59.7	2.3	0.3	2.8	159	2477
Pre-Py JDBC22-4–5 *(n = 16)*															
Min	10.6	0.1	39.0	0.1	0.4	3.3	1.3	0.4	3.5	0.4	1.1	0.3	0.2	49.0	146
Max	16.8	2.6	5094	1.1	0.7	457	98.2	14.6	2364	124	236	13.9	2.0	444	15,099
Average	12.6	1.0	1648	0.4	0.6	69.8	31.7	5.4	462	15.9	40.2	3.2	0.7	233	4365
SD	1.8	1.0	1700	0.4	0.1	126	26.7	4.5	712	30.8	65.3	3.7	0.7	132	3724
Pre-Py JDBC27-2b *(n = 14)*															
Min	38.5	0.2	48.8	0.02	0.2	0.3	5.3	0.1	6.7	0.2	0.0	0.7	0.1	60.4	154
Max	51.8	1.0	4434	3.5	5.1	2.1	56.0	11.9	16,674	54.9	2.6	2.5	2.3	1390	7743
Average	44.6	0.4	1588	0.5	1.2	0.9	25.8	2.8	2185	10.7	0.4	1.3	0.5	396	2462
SD	4.4	0.2	1294	1.0	1.5	0.8	12.8	4.1	4119	15.6	0.7	0.9	0.7	356	2556
Pre-Py JDBC9-2-1a *(n = 5)*															
Min	11.6	0.2	13.8	0.2	BDL	3.2	2.1	0.5	1378	0.1	4.0	7.1	7.8	31.9	4860
Max	13.5	0.3	89.0	4.8	BDL	5.7	13.6	0.7	2202	3.3	7.6	16.2	12.4	82.1	8919
Average	12.4	0.2	51.8	1.2	BDL	4.7	7.8	0.6	1764	1.0	5.7	10.3	10.1	54.3	6124
SD	0.7	0.0	32.5	1.8	BDL	1.0	4.7	0.1	266	1.3	1.5	3.3	1.6	19.7	1594
Py1 JDBC8-2 *(n = 9)*															
Min	47.6	0.4	21.1	1.9	0.7	16.2	15.6	0.2	136	3.1	6.5	3.0	6.1	17.1	3753
Max	190	2.2	146	219	171	1345	1199	1.1	8140	574	184	73.7	32.8	881	82,963
Average	80.7	1.0	56.0	64.1	57.3	648	334	0.6	3134	123	94.5	22.0	19.8	367	16,809
SD	42.9	0.7	36.3	68.2	59.7	422	429	0.4	2787	165	60.8	21.2	10.3	311	23,800
Py-3 JDBC9-2-1b *(n = 6)*															
Min	9.7	0.1	77.0	0.4	4.1	12.5	11.5	0.1	1490	0.9	24.1	0.5	1.5	42.0	1024
Max	21.9	0.6	148	122	52.9	261	2290	0.3	17,602	35.7	89.8	8.7	56.6	110	6121
Average	13.2	0.3	102	71.2	35.4	93.8	779	0.2	9611	9.5	41.8	5.0	17.9	68.4	3845
SD	4.1	0.2	22.6	46.9	19.0	86.4	1051	0.1	5708	12.3	22.3	3.4	19.3	21.6	2056

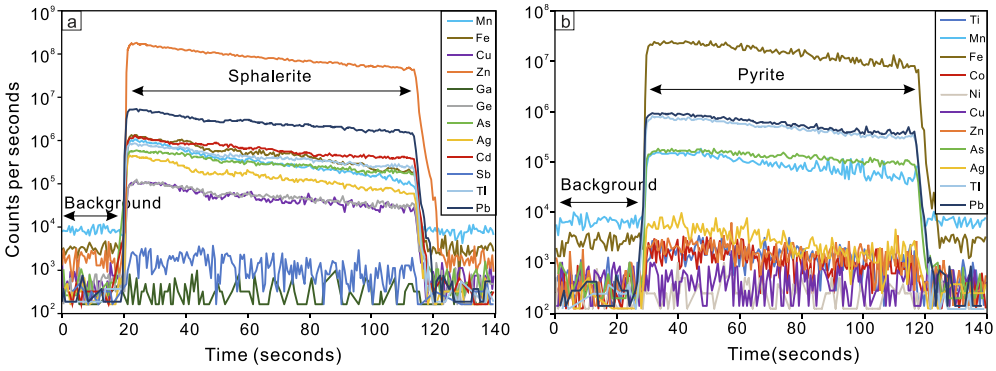

Fig. 6. Transient signal responses for selected elements obtained from LA-ICP-MS analysis for sphalerite (a) pyrite (b). Note no obvious mineral microinclusions are shown in the analysis.

colloform Sp2 is overgrown or enveloped to the galena (Fig. 4f, 5e) and pyrite (Fig. 5f), or early pre-Py or Py1 along the grain margins (Fig. 5a). Sp2 has strong concentric zoning structures (Fig. 5d-g).

The late ore stage is dominated by coarse-grained sulfides. These sulfides consist of translucent euhedral crystalline sphalerite (Sp3), and large, euhedral galena (Gn3) and pyrite crystals (Py3). Paragenetic Cal-II is characterized by oscillatory zones and has annular cathodoluminescence (CL) color (Mu et al., 2021). They are generally filling in the cavities of breccias. Coarse-grained galena-calcite veins that crosscut the early-stage sphalerite-calcite veins indicate late precipitation (Fig. 5h).

The post-ore stage is not related to mineralization and occurs as

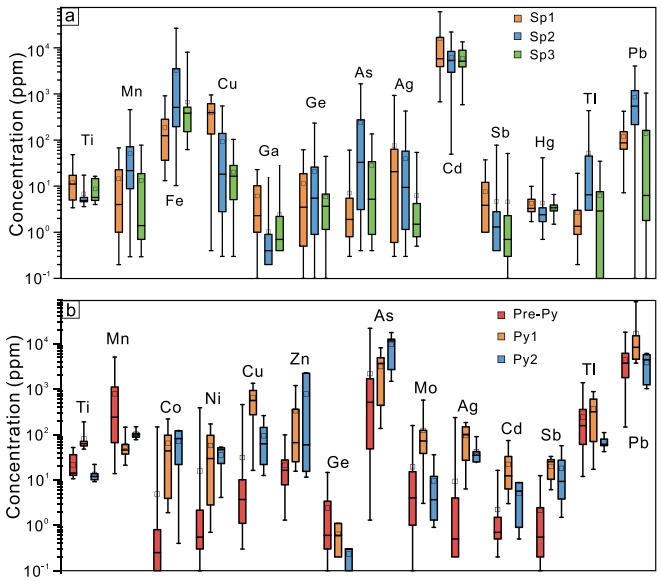

Fig. 7. Box plots for range and mean trace element concentrations for the different sphalerite (A) and pyrite (B) generations at Jinding. Whiskers of boxplots represent the maximum and minimum of data, box edges represent 25th and 75th percentiles, inner lines represent medians, and squares represent means.

minor amounts of calcite and gypsum. This stage was thought to be related to supergene oxidation that calcite and gypsum formed by the dissolution and reprecipitation of these minerals from earlier stages. Calcite (Cal-III) commonly overgrows cores of Cal-I or Cal-II crystals as thin rims (0.1–1 mm thickness) and have younger ages (Mu et al., unpublished data). Oxidized ores generally occur in the shallow cataclastic zone of faults and are composed mainly of smithsonite, cerussite, hydrozincite, strontianite, calamine, and limonite.

4. Sample and methods

Representative samples were collected from surface exposures in Beichang mine and from drill cores in Paomaping mine of the NO.1 orebody at an elevation between 2140 m and 2570 m (Fig. 2). Sampling sites of sphalerite and pyrite bearing in the surface and pit are shown in Fig. 2 and Fig. 3. Samples were prepared as standard polished thin sections for transmitted light analysis and thick (0.5 mm) polished sections for trace element analysis and sulfur isotope work. The analyzed minerals contain disseminated, colloform, and crystalline sphalerite and pyrite formed at different stages of Jinding.

4.1. Trace element spot and mapping analyses

Trace element concentrations were determined by LA-ICP-MS using a GeoLas-Pro 193-nm ArF excimer LA system coupled to an Agilent 7900 quadrupole mass spectrometer at the State Key Laboratory of Ore

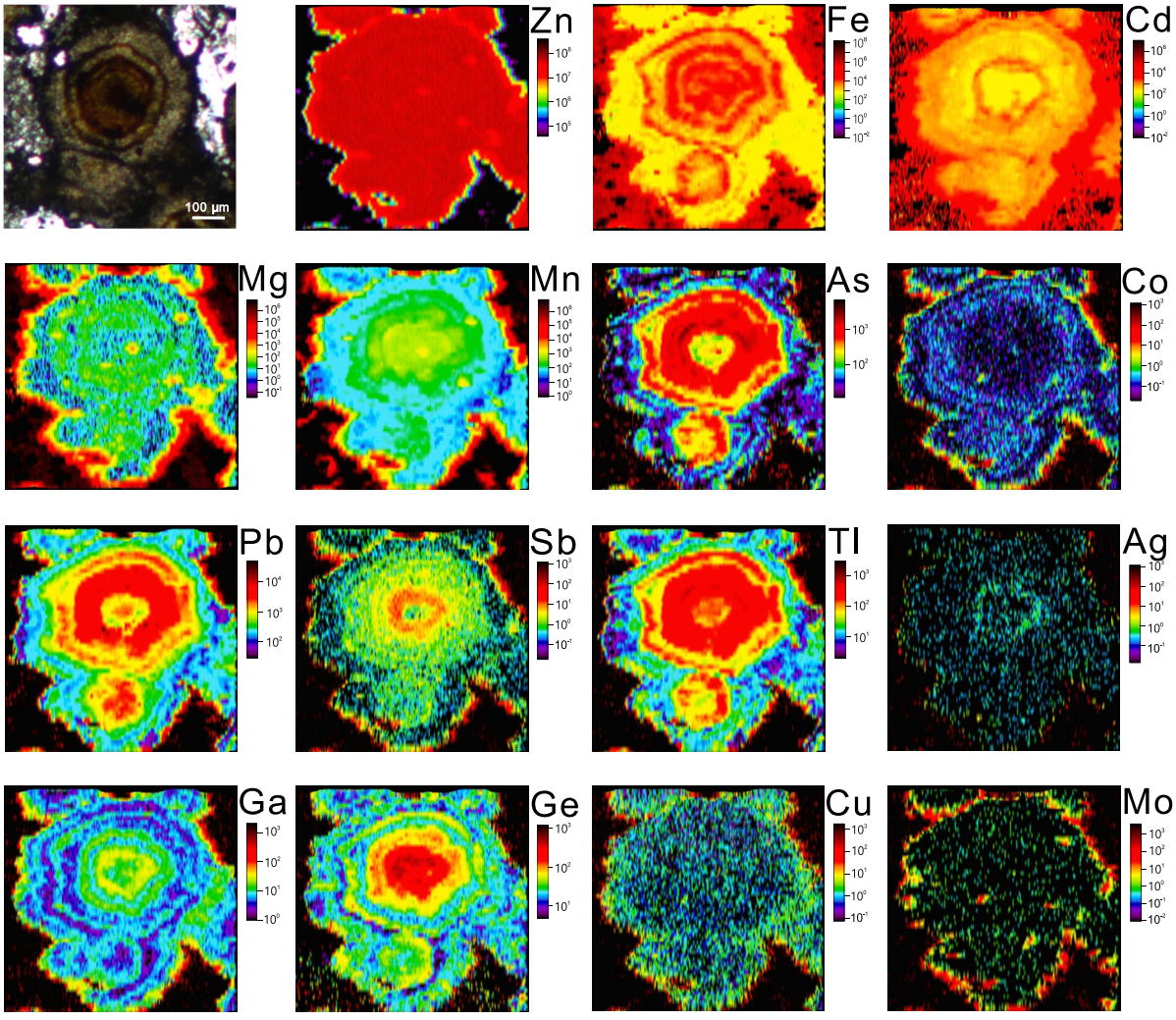

Fig. 8. LA-ICP-MS images of trace elements in colloform sphalerite, sample JDBC21-11-2. The maps show the zonation of various elements from the core to the rim.

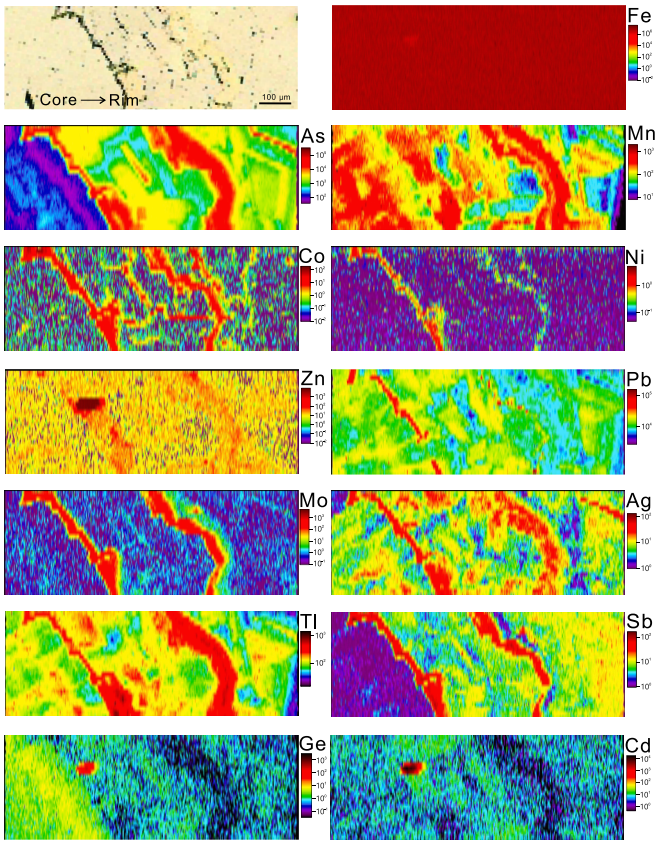

Fig. 9. LA-ICP-MS images of trace elements in pyrite sample JDBC22-5-1. Note the deep red core in the narrow-zoned band is sphalerite inclusions. (For interpretation of the references to color in this figure legend, the reader is referred to the web version of this article.)

Deposit Geochemistry, Institute of Geochemistry, Chinese Academy of Sciences. In this study ^{49}Ti, ^{55}Mn, ^{57}Fe, ^{59}Co, ^{60}Ni, ^{65}Cu, ^{66}Zn, ^{71}Ga, ^{74}Ge, ^{75}As, ^{85}Rb, ^{86}Sr, ^{95}Mo, ^{107}Ag, ^{111}Cd, ^{118}Sn, ^{121}Sb, ^{202}Hg, ^{205}Tl and ^{208}Pb were determined in sphalerite and pyrite. Ablation was carried out using a 26 to 40 μm spot size at 3 to 4.5 J/cm^2. Single spot analyses were ablated using a repetition rate of 6 Hz. Helium was used as a carrier gas during the whole ablation and was mixed with argon before entering the ICP-MS. The analyses were performed in time-resolved mode with each spot consisting of 20 s background measurement, 60 s signal measurement, and 40 s elimination of memory effect. For data reduction, signal integration and calibration of the LA-ICP-MS data were performed using the LADR software (http://norris.org.au/ladr/). The calibration of sphalerite is carried out by the normalization method with STDGL3 (FeSb) as an external standard. For pyrite, Fe as determined by electron probe microanalysis (EPMA) was used as the internal standard, and a known FeS as the external standard. Other elements were calibrated and converted by GSE-1G and GSD-1G. The sulfide reference material MASS-1 (Wilson et al., 2002) was used as the calibration standard. Inclusions of sulfides were excluded from the time-resolved spectrum before calculating the average signal.

Trace element mapping of sphalerite was prepared for Fe, As, Zn, Cu, Cd, Tl, Ag, and Pb, which was performed by ablating sets of parallel line rasters in a grid across the sample. The lines were ablated with a repetition rate of 15 Hz, beam size of 10 or 15 μm, and rastering at 15 μm/s to achieve optimal coordination of image spatial resolution, detection limits, and acquisition time. A delay of 20 s after each line was used to cell wash out. Background levels and the reference materials standard (same as spot analysis) were measured before and after each image to calculate element concentration and assess drift. Element maps were undertaken according to IgorPro Iolite 3.0 program (Paton et al., 2011; Danyushevsky et al., 2011).

4.2. Sulfur isotopes

In-situ sulfur isotopic analyses were carried out using a Nu Plasma III MC-ICP-MS (Nu Instruments) attached to a RESOlution-155 ArF193-nm laser ablation system (Australian Scientific Instruments) at State Key Laboratory of Ore Deposit Geochemistry, IGCAS. S isotopic analyses were performed on repolished sections that analyzed LA-ICP-MS trace elements. Sulfide was ablated in a mixture of helium (350 ml/min) and nitrogen (2 ml/min) atmosphere using 40–60 μm spot size, 6 Hz repetition rate, and 2 J/cm^2 energy density. The sulfur isotope data (^{32}S, ^{34}S) were collected in static mode. Each analysis comprised 20 s baseline time, 40 s ablation time, and 40 s wash time. Pyrite pressed powder tablet (PSPT-2) was used for external standard bracketing (Bao et al., 2017, Chen et al., 2019). Two in-house standards consisting of nature pyrite crystals (SB-1 from Shangbao W-Sn deposit yielded the value of $\delta^{34}S_{CDT}$ (‰) of 16.57 ‰ (n = 12) and HYC-1 from Huayangchuan Nb-U-REE deposit, China yielded the value of $\delta^{34}S_{CDT}$ (‰) of −5.76 ‰ (n = 12) were used for quality control after every five unknown samples.

5. Results

5.1. Trace element composition and mapping

A summary of trace element compositions of sphalerite and pyrite data determined by LA-ICP-MS is given in Table 2 and Table 3, respectively. The time-invariant trace of the spot analysis for the LA-ICP-MS counts output by laser ablation indicates that trace elements are most probably contained as a solid solution in sphalerite rather than as inclusions (Fig. 6). In this study, Fe, Cd, Co, Ga, Ge, In, Mn, As, Pb, Sb, and Tl are present in solid solutions that are used to identify the range of concentrations and correlation trends. Some ragged spectra show the presence of Pb, Ag, and Cu micro-inclusions of minerals. The complete dataset for each sample is in the electronic Appendix Table A1. The data include 3 samples for disseminated sphalerite, 7 samples for colloform sphalerite, and 3 samples for crystalline sphalerite, A total of 215 spots were determined.

The disseminated sphalerite (Sp1) is commonly enriched in metal elements Fe (13.2–907.7 ppm, 188.4 ppm on average), Pb (7.2–420.5 ppm, 119.8 ppm on average), Ag (0.3–927 ppm, 75.5 ppm on average), and Cu (0.4–951 ppm, 387 ppm on average). In addition, critical metals Cd (675–60560 ppm, 15559 ppm on average), Ge (0.1–61.3 ppm, 11.5 ppm on average), Ga (0.1–22.8 ppm, 6.1 ppm on average), Sb (0.2–37 ppm, 7.8 ppm on average), and Tl (0.2–19 ppm, 2.7 ppm on average) are also enriched in the disseminated sphalerite, especially for Cd.

The colloform sphalerite (Sp2) has a more scattered and wide range of trace element contents as a result of the variation in the mineral growth zone. The different colors of zonations from the colloform sphalerite (Fig. 5) have variable trace element compositions, especially for elements Cd and Fe. Trace element plots (Fig. 7) show that colloform sphalerite has relatively enriched in Fe (10.5–26572 ppm, 3228 ppm on average), As (0.4–1659.4 ppm, 236.8 ppm on average), Ge (0.1–233.5 ppm, 20.7 ppm on average), Pb (10.5–26572 ppm, 3228 ppm on average) and Tl (10.5–26572 ppm, 3228 ppm on average), and relatively lower in Cu (0.3–548.5 ppm, 92.2 ppm on average), Cd (49.4–22041 ppm, 6187 ppm on average) and Ga (0.1–15.3 ppm, 1.1 ppm on average) compared to Sp1 and Sp3.

The crystalline sphalerite (Sp3) has a relatively lower concentration in Cu (0.3–103.2 ppm, 20.2 ppm on average), Cd (585.6–13468 ppm, 5944 ppm on average), Pb (0.1–1040 ppm, 136.5 ppm on average) and Ag (0.5–53.9 ppm, 6.3 ppm on average). The critical metals for Sp3 show Ge ranging from 0.1 to 44.2 (mean 5.8 ppm), Ga ranging from 0.1 to 27.9 ppm (mean 2.5 ppm), Sb ranging from 0.1 to 51 ppm (mean 4.5 ppm), and Tl ranging from 0.1 to 34.7 ppm (mean 6.2 ppm), respectively.

Table 4
Sulfur isotopes data of sphalerite from Jinding deposit.

Sulfide	Sample no.	δ^{34}S(VCDT)	2SE	Sulfide	Sample no.	δ^{34}S(VCDT)	2SE
Disseminated sphalerite (Sp1)	JDBC8-2	−18.78	0.19		Sp-jdbc21-5	−19.43	0.17
		−19.54	0.19			−20.14	0.19
		−17.57	0.19			−18.30	0.19
		−17.70	0.19			−18.44	0.20
		−21.03	0.20			−18.00	0.19
		−17.70	0.20			−17.80	0.26
		−17.87	0.19		JDBC22-4–5	−21.86	0.19
		−20.71	0.19			−17.30	0.19
	JDBC16-2	−19.05	0.19			−16.10	0.20
		−18.43	0.18			−18.29	0.19
		−22.10	0.19			−16.49	0.20
		−20.83	0.19			−18.30	0.20
		−21.29	0.20			−17.70	0.20
		−18.22	0.20			−18.62	0.20
		−22.74	0.17			−12.56	0.20
Nodular aggregate sphalerite (Sp2)	JDPMP-1–1-3	−1.20	0.17			−16.16	0.19
		−1.01	0.19			−16.02	0.19
		−1.68	0.18			−17.60	0.19
		−2.54	0.18		JDBC9-2-1o	−21.43	0.18
		−2.42	0.18			−21.71	0.19
		−1.27	0.19			−28.41	0.19
		−1.59	0.18			−26.35	0.19
		−0.49	0.19			−22.90	0.19
Colloform sphalerite (Sp2)	JDBC22-6–4	−17.34	0.17			−24.01	0.18
		−18.33	0.17	Crystalline sphalerite (Sp3)	JDBC9-2-1y	−20.93	0.18
		−18.74	0.19			−20.45	0.17
		−16.77	0.20			−20.63	0.18
		−20.10	0.20			−21.12	0.18
	JDBC21-5–1	−25.16	0.19			−21.26	0.17
		−23.12	0.20			−20.46	0.18
		−22.08	0.20		JDBC22-6-4y	−18.16	0.19
		−23.12	0.18			−18.91	0.19
		−21.82	0.19			−17.62	0.19
		−22.09	0.18			−19.05	0.19
		−21.62	0.20			−17.67	0.19
		−18.12	0.19			−18.05	0.21

Pre-ore pyrite, commonly tubercular and colloform, is more abundant than Py1 and Py2 in the Jinding deposit. Pre-ore py is characterized by depleted in elements Co, Ni, Cu, Zn, As, Mo, Ag, Cd, Sb, and Ag compared to ore stage Py1 and Py2, while having relatively high-grade Mn concentration ranging from 13.8 to 5094 ppm (mean 788 ppm) (Fig. 7). Ore stage pyrite Py1 and Py2 have distinct high metal content of Pb varying from 3753 to 82963 ppm with a mean of 16,809 ppm and 1024 to 6121 ppm with a mean of 3845 ppm, respectively. Zn content in Py1 and Py2 are also high varying from 15.6 to 1199 ppm with a mean of 334 ppm and 11.5 to 2290 ppm with a mean of 1051 ppm, respectively.

Individual textural and chemical patterns for the sphalerite sample were mapped in detail with the LA-ICP-MS mapping for this study. LA-ICP-MS mapping highlights the complex zoning revealed by etching and shows that each zone has a different trace element chemistry (Large et al., 2009). The sample consists of zonation, which is one of the most representative in this deposit. Trace element image results show that colloform sphalerite has clear growth zoning in Fe, Cd, Mg, Mn, As, Co, Pb, Sb, Tl, Ag, Ga, and Ge, except for elements Cu and Mo (Fig. 8). These element concentrations are relatively enriched and depleted in different zonation. The concentration is varied by one or two orders of magnitude in different zoning. For example, in the case of sphalerite JDBC21-5-1a and JDBC22-4–5 where Cd concentration varies up to an order magnitude within 10 to 100 μm of sphalerite growth (Figs. 11–13). The inverse relation in trace element concentrations between Cd and Fe is clearly displayed in the LA-ICP-MS trace element maps of a colloform sphalerite grained (Fig. 8). The narrow-zoned overgrowth and core zone are relatively enriched in Fe, As, Pb, Tl, Ga, and Ge compared to the wide-zoned, which contains Cd and Sb in the sample JDBC11-8. Concentrations of Ga, Ge, Sb, and Tl are also documented by the LA-ICP-MS mapping of these sulfides, suggesting that the hydrothermal fluid carried some critical metals, especially in the dark core of colloform sphalerite grained.

Pyrite aggregates in the sample JDBC22-5-1 have been mapped by the LA-ICM-PS imagining technique (Fig. 9). The map indicates varied zonation of trace elements from core to rim of the pyrite. Most of the elements are low in pyrite core, followed by elevated in the surrounding zone, except element Ge. Two thin rims (<70 μm) are apparent on the surrounding zone of the pyrite. LA-ICP-MS images of pyrite show variations of trace elements in the pyrite growth band in As, Mn, Co, Ni, Zn, Pb, Mo, Ag, Tl, Sb, Ge and Cd (Fig. 9). The narrow-zoned py band is relatively enriched in As, Mn, Co, Ni, Mo, Ag, Tl, Sb, but is depleted in Ge and Cd. The images show that Ge is enriched in the inner growth band of pyrite, where As and Sb display a relative depletion trend.

5.2. Sulfur isotope compositions of sulfides

The sulfur isotope compositions via in situ LA-MC-ICP-MS are presented in Table 4 and Table 5 andgraphically illustrated in Fig. 10. The results reveal a relatively consistent trend in S isotopes from Sp1 to Sp3 and show some notable variation in some samples. The δ^{34}S values of the fifteen analyses of disseminated sphalerite (Sp1) show a range of –22.7 to −17.6 ‰ with a mean δ^{34}S of −19.6 ‰ (s.d. = 1.74, n = 15). Colloform sphalerite (Sp2) has a relatively uniform range of sulfur isotope compositions in samples JDBC22-6-co, JDBC22-4–5, JDBC21-5-1a, and JDBC9-2–1 ranging in δ^{34}S from −28.4 to −12.6 ‰ (mean = -19.8 ‰, s.d. = 3.3, n = 37). Distinctively light δ^{34}S in a narrow range of −2.5 to −0.5 ‰ (mean = -26.3 ‰, s.d. = 3.8, n = 5) are found in sample JDPMP-1–1-3 of nodular aggregates Sp2. Compared to the replaced calcite colloform sphalerite, the JDPMP-1–1-3 nodular sphalerite replaced gypsum. Crystalline sphalerite (Sp3) that deposited later after colloform

Table 5
Sulfur isotopes data of pyrite from Jinding deposit.

Paragenetic sequence	Sample no.	δ^{34}S(VCDT)	2SE	Paragenetic sequence	Sample no.	δ^{34}S(VCDT)	2SE
Disseminated pyrite (Py1)	JDBC8-2	−28.75	0.18			−16.39	0.17
		−30.47	0.17			−15.76	0.17
		−16.30	0.18			−15.67	0.17
		−16.96	0.18			−12.64	0.16
		−30.33	0.21			−12.43	0.17
		−30.14	0.19			−12.95	0.17
		−17.93	0.20			−11.18	0.16
		−32.11	0.18		Py-bc21-5-1b	−9.66	0.16
		−31.24	0.17			−15.41	0.16
		−16.88	0.18			−14.22	0.16
		−31.71	0.20			−11.04	0.16
		−23.90	0.19			−11.63	0.16
		−31.97	0.22			−11.76	0.17
		−17.70	0.21			−12.10	0.17
Pre-ore pyrite	JDBC16-2	−14.12	0.23			−13.05	0.17
		−7.68	0.19			−12.44	0.17
		−9.31	0.17			−15.39	0.17
		−18.50	0.18			−16.13	0.17
		−18.74	0.18			−15.64	0.17
		−15.45	0.18			−14.19	0.17
		−15.05	0.18			−13.81	0.17
		−16.51	0.18			−14.49	0.18
		−17.95	0.18			−15.44	0.17
		−17.05	0.18			−16.20	0.17
		−11.36	0.19	Pre-ore euheddral pyrite	JDBC9-2-1n	−2.40	0.18
		−18.47	0.17			0.84	0.18
	JDBC22-4–5	−9.16	0.17			1.74	0.18
		−8.38	0.16			−4.56	0.17
		−8.71	0.16			−2.59	0.17
		−8.84	0.15			−0.50	0.18
		−8.19	0.16			−4.02	0.18
		−8.84	0.17			−5.75	0.19
		−10.00	0.17	Crystalline Pyrite (Py2)	JDBC9-2-1w	−16.54	0.18
		−10.73	0.16			−17.93	0.19
		−12.09	0.16			−15.67	0.20
		−10.66	0.16			−13.17	0.19
		−11.20	0.17			−14.85	0.24
		−13.47	0.18			−15.01	0.19
		−14.10	0.15			−15.82	0.21
		−11.73	0.16			−18.17	0.18
		−11.13	0.16			−15.33	0.20
	JDBC21-5-1a	−10.38	0.17			−14.62	0.22
		−14.65	0.16			−15.47	0.23
		−16.29	0.17			−15.67	0.20

VCDT = Canyon Diablo Troilite.

sphalerite (Sp2) has similar sulfur isotope compositions ranging in δ^{34}S from −21.5 to −17.6 ‰ (mean = -19.5 ‰, s.d. = 1.4, n = 12; Fig. 10a).

S isotopes in pyrite from pre-ore py to py2 show a notable variation. Pre-ore colloform pyrite in samples JDBC16-2, JDBC22-4–5, JDBC21-5-1a have δ^{34}S values ranging from −18.7 to −7.7 ‰ with a mean of −13.1 ‰ (s.d. = 2.9, n = 54). Fourteen spot analyses on disseminated py1 show a relative variation in δ^{34}S values from –32.1 to −16.3 ‰ with a mean of −25.5 ‰ (s.d. = 6.7). The euhedral pyrite core in sample JDBC9-2–1 has a δ^{34}S ranging from −5.8 to + 1.7 ‰ with a mean of −2.2 ‰ (s.d. = 2.7), whereas the δ^{34}S signature remarkably decreases from −18.2 to −13.2 ‰ with a mean of −15.7 ‰ (s.d. = 1.4) on the pyrite rim area, compared to the earlier pyrite hydrothermal generations (Fig. 10b).

6. Discussion

6.1. Element correlation trends and substitution

The dataset correlation trend between minor and trace elements (Fe, Cd, Ge, Mn, Pb, Cu, Ag, Tl, Sb, etc.) reveals their coupled substitution mechanisms in sphalerite. Fe and Cd show a significant negative correlation (Fig. 14a). A Fe/Cd ratio equal to 1 is characteristic of the simple substitution mechanism and can be proposed substitution equations: $Cd^{2+}\leftrightarrow Zn^{2+}$, $Fe^{2+}\leftrightarrow Zn^{2+}$, and $Cd^{2+}\leftrightarrow Fe^{2+}$ substitution.

The good correlation between Fe and Ge seen in the Jinding sphalerite (Fig. 14b) across the full dataset indicates that germanium is preferentially incorporated within high-Fe-sphalerite and raises the possibility of a coupled substitution involving Fe and Ge. These positive correlations are also shown between Ge and several cations which are commonly known as divalent in the sphalerite system (Mn^{2+}, and Pb^{2+}; Figs. 11, 12), but no correlation with monovalent cations (Cu^{+}, Ag^{+}; Figs. 11, 12) in the Jinding deposit. These correlations are similar to the Tres Marias Zn deposit, suggesting that the Ge is incorporated as Ge^{4+} in the natural sphalerite on the basis of XANES spectra (Cook et al., 2015, Liu et al., 2023). The simple mechanism of substitution should be Ge^{4+}+ (vacancy) ↔ $2Zn^{2+}$ and $2Fe^{2+}+Ge^{4+}\leftrightarrow 4Zn^{2+}$. Another possibility is a simple substitution of Ge in a reduced state (Ge^{2+}), which might be directly substituted as $Ge^{2+}\leftrightarrow Zn^{2+}$ (Cook et al., 2009; Ye et al., 2011; Belissont et al., 2014).

Mn and Pb are positively correlated with Fe, which can be assumed as simple substitutions of the bivalent cation. The coalescence of Mn^{2+} ions to form clusters may be one of the reasons for the banded pattern in sphalerite crystals (Di Benedetto, 2005; Cook et al., 2009). A positive correlation of As and Tl with Fe is also observed. Tl and As are most likely incorporated in low-temperature, reducing conditions where organic material might be involved (Pfaff et al., 2011 and therein).

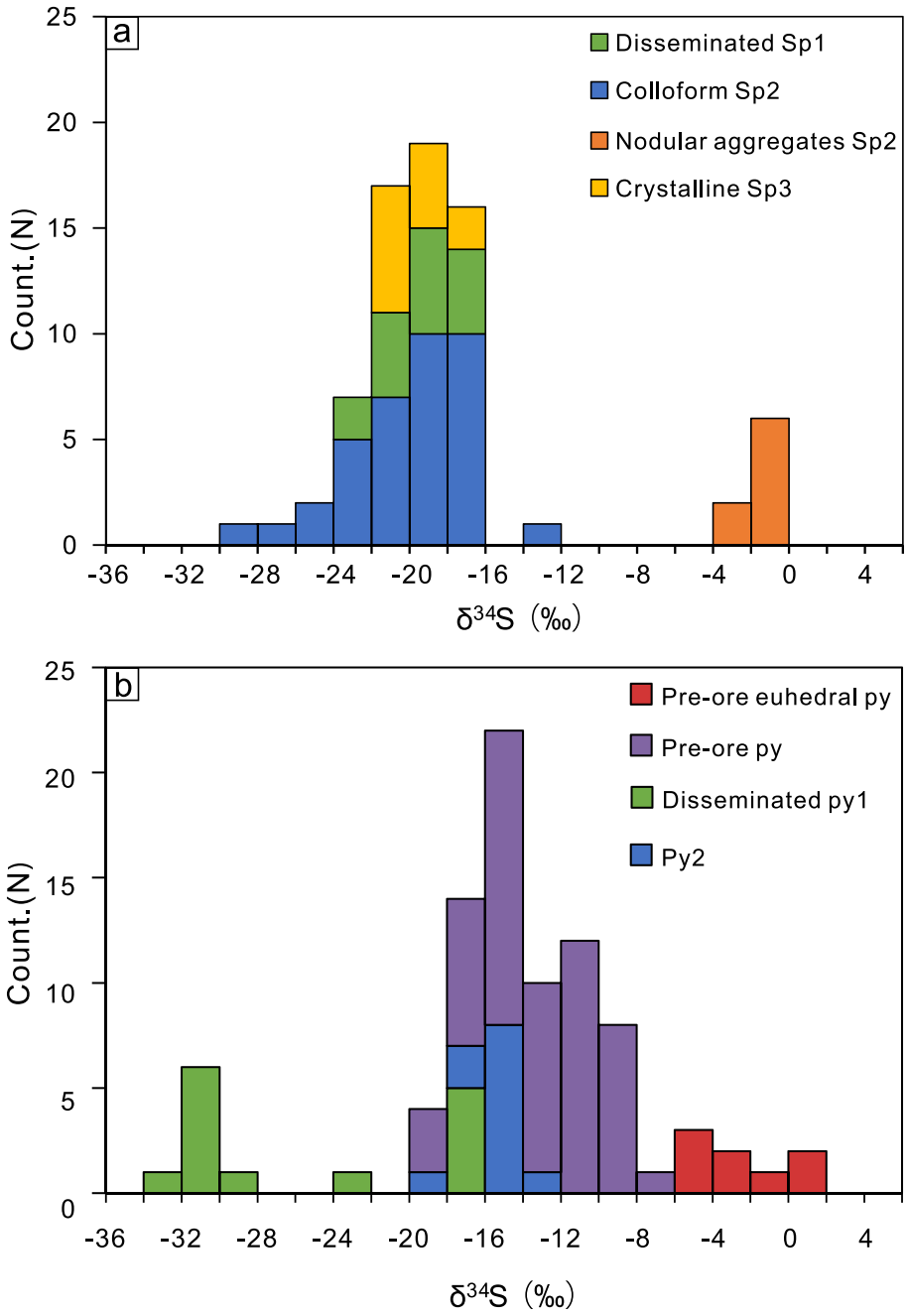

Fig. 10. Histograms showing a range of sulfur isotope values of various generations of pyrite (a) and marcasite (b) at Jinding.

A strong correlation between Fe and Ge + Mn + Pb + As + Tl along the 1/1 (Fig. 14g) highlights a general coupled substitution for trace elements incorporated into sphalerite. Johan (1988) proposed that coupled substitution mechanisms for trivalent and tetravalent elements (Ge^{4+}, As^{3+}, and Tl^{3+}) in sphalerite is a possible need for the formation of donor–acceptor pairs with monovalent ions (Ag and/or Cu). However, the Jinding deposit shows no enrichment in monovalent ions coupled substitution here. Hydrothermal sphalerite synthesis experiments by Liu et al., (2023) reveal that Ge^{4+} substitution in sphalerite occurs with and without the presence of other metal ions (e.g., Cu^{+}). Therefore, our data obtained support the simple substitution or via vacancies as well as coupled substitution mechanisms for minor elements in sphalerite. We suggest possible substitution mechanisms for the incorporation of Fe-related elements into the sphalerite lattice: $Fe^{2+}+Ge^{4+}+Mn^{2+}+Pb^{2+}+As^{3+}+Tl^{3+}+(\text{vacancy}) \leftrightarrow 8Zn^{2+}$.

The oxidation state of Cu and Ag as solid solution in sphalerite is likely the monovalent, Sb likely exists in the trivalent, respectively (Pattrick et al., 1993; Cook et al., 2009; Ye et al., 2011; Liu et al., 2023). In this study, Cd and Cu, Ag, and Sb show weak positive correlations, respectively (Fig. 15a-c). Cu and Ag, Sb show good correlations (Figs. 11-13), which may suggest coupled substitution expressed as $Cu^{+}/Ag^{+}+Sb^{3+}\leftrightarrow 3Zn^{2+}$. The weak correlation is possibly attributed to the presence of submicron to nano-scale Cu-Ag-Sb-bearing inclusions of other sulfides or sulfosalts, but for entering solid solution completely. The weak correlation between Cd and Cu/Ag + Sb in the dataset (Fig. 15d) suggests a possible role for a limited degree of Cu/Ag + Sb couple substitution, with the nano-scale inclusions of Cu-Ag–Sb-bearing minerals. The possible substitution mechanisms for the incorporation of Cd-related elements into the sphalerite lattice: $Cd^{2+}+Cu^{+}+Ag^{+}+2Sb^{3+}\leftrightarrow 5Zn^{2+}$.

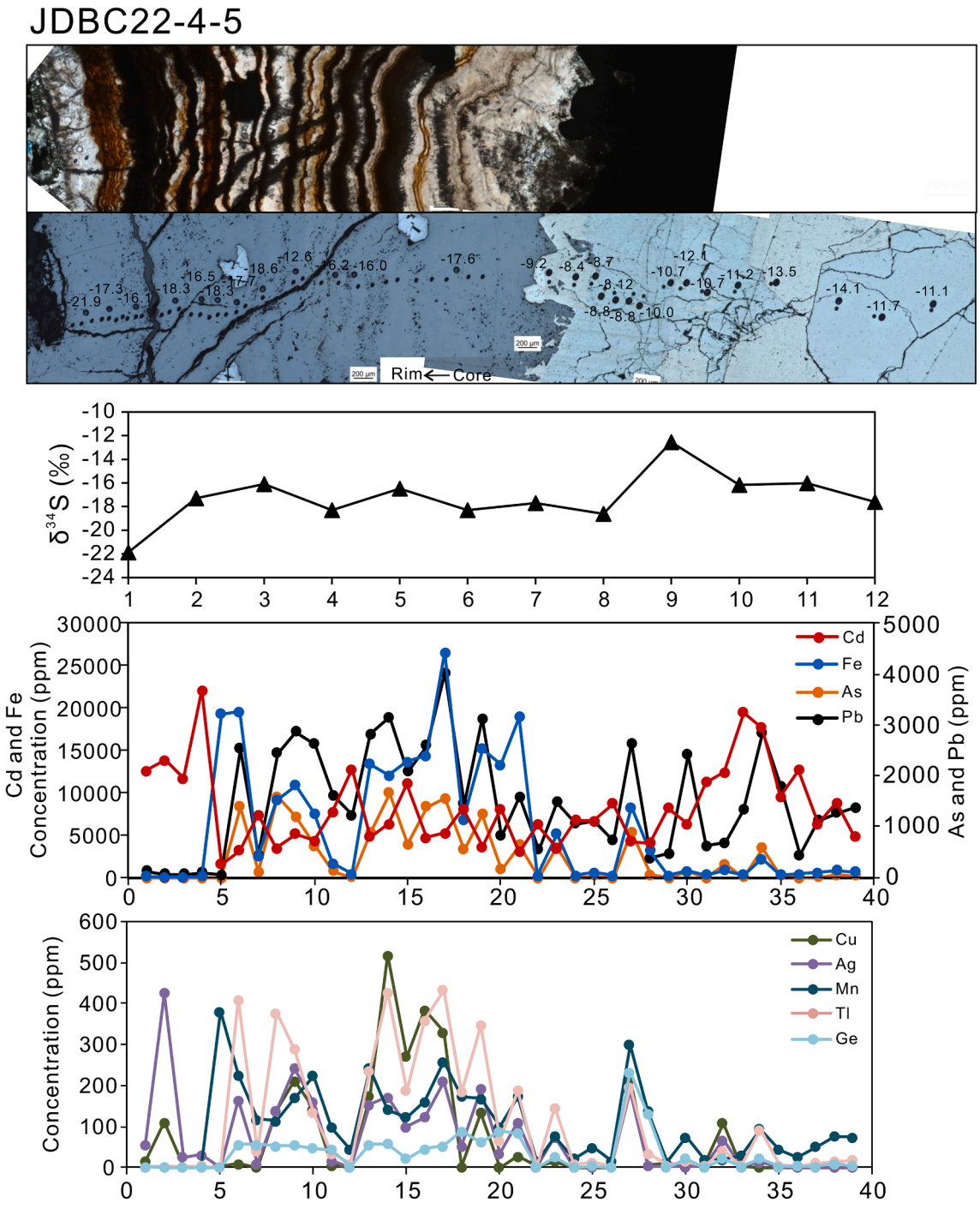

Fig. 11. Detailed traverses obtained for samples JDBC22-4–5 based on the sulfur isotope and trace element compositions.

As mentioned above, correlations between Fe, Cd, and other individual elements described in this study suggest that the incorporation of trace elements is facilitated by the replacement of Zn by Cd and Fe.

6.2. Sample-scale color and chemical composition variations

Trace element mappings and individual LA-ICP-MS geochemical traverses across individual layered sphalerite and pyrite at Jinding show oscillatory zonation and rhythmic banding at the scale of the micrometer in individual sample layering (Figs. 8-13). These distinct chemical composition variations and color zoning are attributed to the incorporation of minor element components in sphalerite (Oen et al., 1980; Kuhlemann and Zeeh, 1995; Beaudoin, 2000; Di Benedetto, 2005; Cook et al., 2009; Pring et al., 2020). In this study, a highly variable color correlation between sphalerite color and element pair Cd and Fe content has been observed, with a significant negative rhythmic correlation band. In the analyzed samples JDBC21-2-5b, JDBC22-4-5, and JDPMP1-3 zones predominantly consist of light-colored sphalerite alternating with thin layers of darker-colored sphalerite (Figs. 11–13). Brown sphalerite always has high Fe, As, Mn and Ge content, while sphalerite rich in Cd and Sb is often pale gray to colorless. Numerous correlations between colors and elements have been reported. Brownish dark sphalerite was suggested to derive from high Fe concentration in the SW Wisconsin MVT deposits (McLimans et al., 1980). Elevated As concentrations also correlate with darker sphalerite in the Wiesloch MVT deposit, Germany (Pfaff et al., 2011) and in the Navan Zn-Pb deposit,

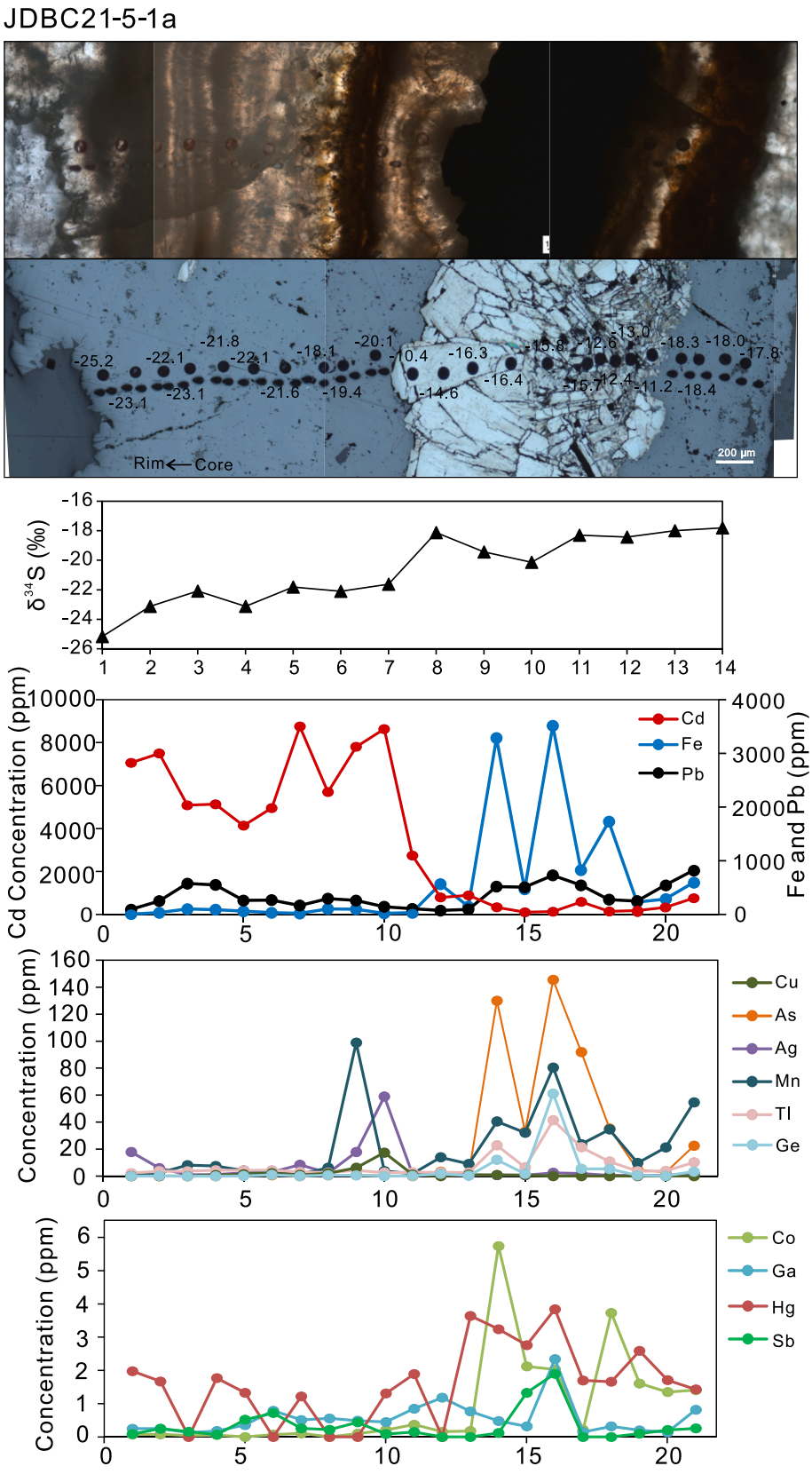

Fig. 12. Detailed traverses obtained for samples JDBC21-5-1a based on the sulfur isotope and trace element compositions.

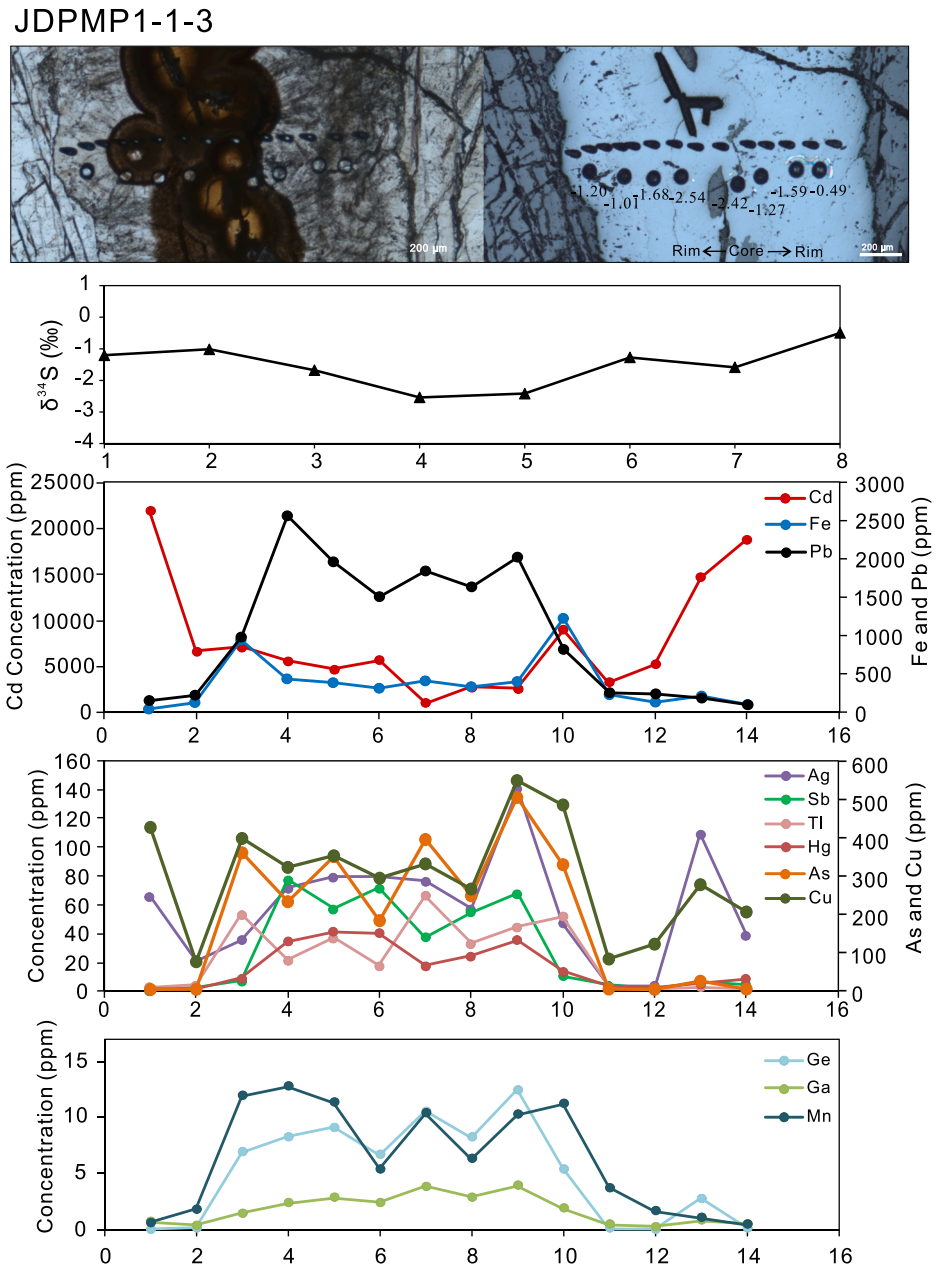

Fig. 13. Detailed traverses obtained for samples JDBCPMP1-1–3 based on the sulfur isotope and trace element compositions.

Ireland (Gagnevin et al., 2014). The presence of Cu, Ge (and Ga) leads to a brownish darkening of the sphalerite in the Tennessee MVT deposit, USA (Bonnet et al., 2016). Our study supports that the dark brown sphalerite ascribed to elevate Fe, As, and Ge content, but it is not clear whether one or several elements are responsible.

Cd and Fe have the highest concentrations of all the minor elements and can be representative of the behavior of other trace metals on the basis of their correlations. In particular, extremely high concentrations of Cd are found in the Jinding deposit, which is rare in other Zn-Pb deposits. The incorporation of Cd in sphalerite is critically influenced by the fluid composition and extent of metal leaching from its source rock. Studies have shown that the amount of Cd in sphalerite may fingerprint the extent of basement-derived (with heavy sulfur) hydrothermal fluid input in the Irish-type deposits (Wilkinson et al., 2005b; Barrie et al., 2009). The hydrothermal sphalerite in Jinding is commonly enriched in Cadmium, and Cd-correlated elements like Sb and Ag and subordinate Cu are also considered to be transported and introduced by basement-derived fluids cooling during their ascent and the concomitant mixing process (Pfaff et al., 2011). Therefore, this study with sphalerite fluid inclusion results (Mu et al., 2021) may emphasize the conclusion that the ore fluids may flow from metal-fertile sedimentary/basement sequences.

Generally, the incorporation and fractionation of Fe in sphalerite are controlled by pressure and/ temperature conditions, pH, or sulfur activity of the fluid (Anderson, 1973; Di Benedetto, 2005; Wilkinson et al., 2005; Pfaff et al., 2010, 2011; Gagnevin et al., 2014; Frenzel et al., 2021). The dependence on temperature can be important in that mineralizing fluids cooling to different degrees would result in changes in the dissociation constants of complexes (Yardley, 2005; Frenzel et al. 2016). The studies of Frenzel et al. (2016) suggest that the concentrations of Ga, Ge, Fe, Mn, and In are proved to be a strong control of sphalerite chemistry by fluid temperature, while the concentrations of Ag, Cd, Co, and Cu appear to be independent of temperature. Due to the abnormally low Fe and Mn content in Sp1 and Sp3 in the Jinding deposit (Fig. 7), the mineral geothermometer GGIMFism is ineffective here, while according to the empirical relationship, we can speculate that the

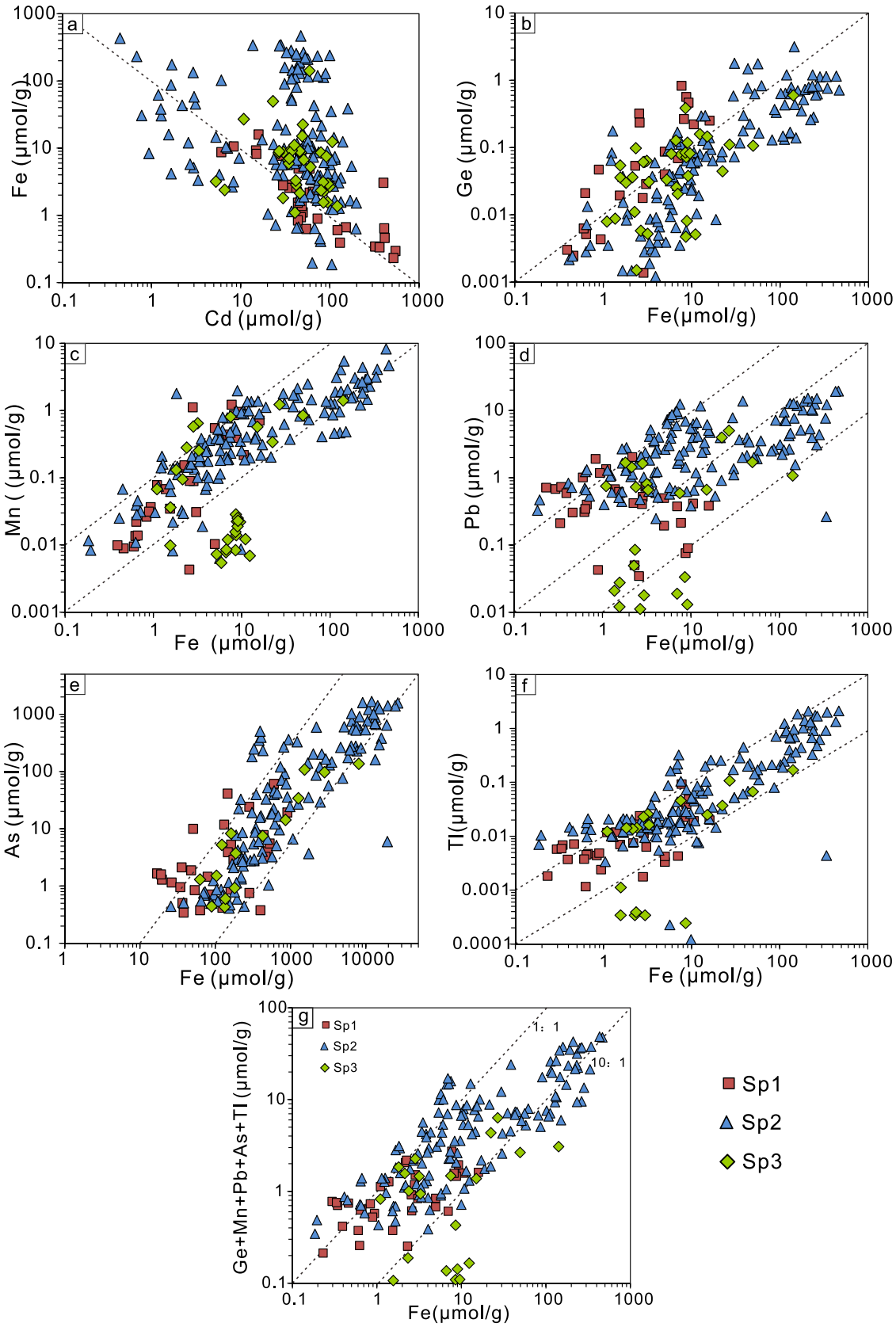

Fig. 14. Correlations plots of Fe versus elements (a) Cd, (b) Ge, (c) Mn, (d) Pb, (e) As, (f) Tl, and (g) Ge + Mn + Pb + As + Tl.

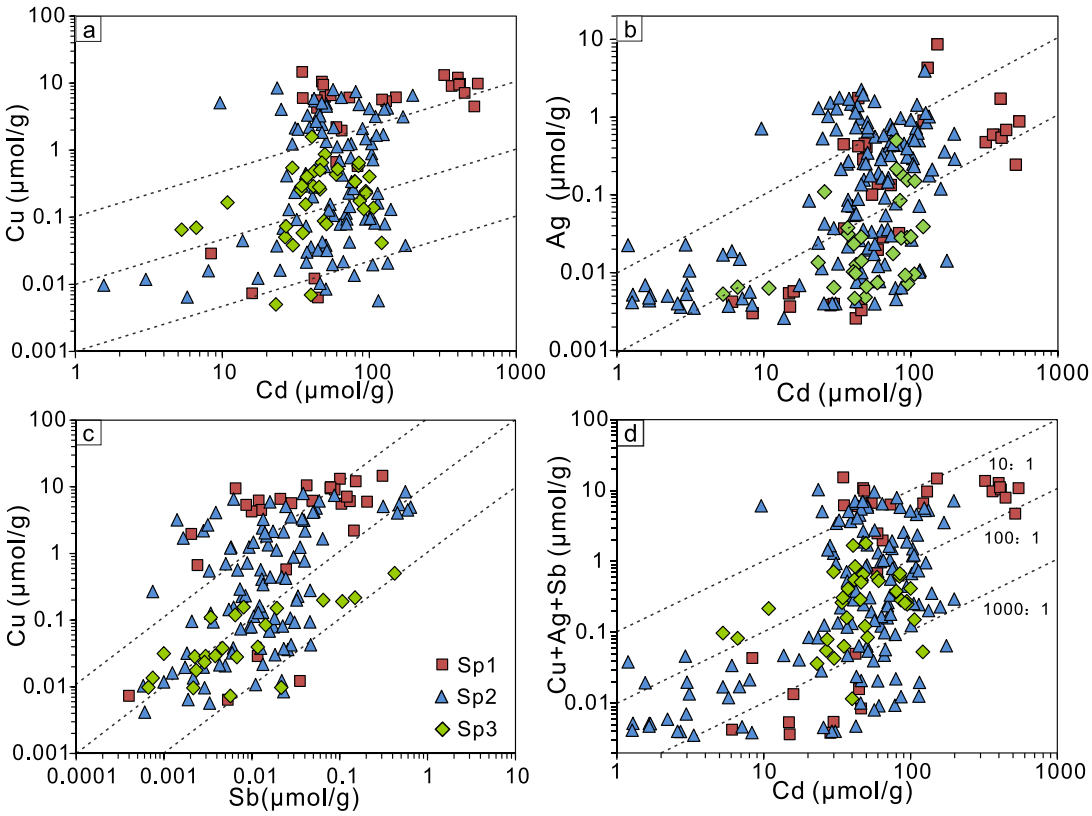

Fig. 15. Correlations plots of (a) Cd versus Cu, (b) Cd versus Ag, (c) Sb versus Cu, and (d) Cd versus Cu + Ag + Sb.

temperature of Sp2 is lower than Sp1 and Sp3. This is in agreement with the homogenization temperature of fluid inclusion in sphalerite that Sp3 has a higher temperature than Sp2 (Mu et al., 2021), probably reflecting temperature control on sphalerite composition. The sulfur activity of the mineralizing fluid for the variation of Fe concentration in sphalerite is discussed in the following part.

6.3. Sphalerite precipitation histories

In the Jinding hydrothermal system, the sulfur isotopic values show high isotope fractionation in the sphalerite (around −28.4 to −12.6 ‰, Fig. 10), which suggests the production of sulfides mainly occurs biological pathways. The Jinding sphalerite formed at temperatures between 79 and 173 °C as indicated by fluid inclusion thermometry (Mu et al., 2021). Considering bacteriogenic sulfate reduction (BSR) predominates at temperatures around and well below 100 °C (Jørgensen, 1979), the reduced sulfur was produced mainly by bacterial reduction of sulfates in the paleohydrocarbons trapped in the cap of the Jinding dome before Zn–Pb mineralization (Tang et al., 2014; Xue et al., 2015; Chi et al., 2017; Mu et al., 2021). Three types of sphalerite in two generations, the early and late, are indicative of growth from bacteriogenic sulfide. The disseminated pyrite, which have generally the lowest $\delta^{34}S$ values (–32.1 to −16.3 ‰), probably represent strongest microbial activities and BSR. The outward decrease in $\delta^{34}S$ in the sphalerite zonations (Figs. 11-13) may reflect increasing microbial activities as the aggregates grew, similar to the aggregates in the Xue et al. (2015).

Bits of nodular sphalerite (Fig. 5d, 13), which has distinctively light $\delta^{34}S$ in a narrow range of −2.5 to −0.5 ‰. This might imply a sulfide mineralization derived from the thermochemical reduction of organic matter. In the salt diapir-related Zn-Pb deposit, sulfur isotopic composition of metal sulfides correlates with the extent of biodegradation of hydrocarbons, base metal content, and the proportion of aromatics in the organic extracts (Bou Jaber salt diapir-related Zn-Pb deposit, Bechtel et al., 1996). Thus the high $\delta^{34}S$ values can be interpreted to reflect bacterial sulfate reduction in a more or less closed system rather than a thermogenic contribution (Bechtel et al., 1996).

The sphalerite LA-ICP-MS data have been compared with the available S isotope data which are able to correspond one to one (in four samples) for recording the fine-scale chemical variations. The chemical signature coupled with the textural appearance at the micrometer scales of layered sphalerite and pyrite, can provide clues to rather complex precipitation histories to Zn-Pb deposits (Barrie et al., 2009; Gagnevin et al., 2014). In the case of sphalerite JDBC21-5-1a (with bacteriogenic affinity; Fig. 10), Fe is correlated with $\delta^{34}S$ ($r^2 = 0.613$; Fig. 16), and Cd is anti-correlated with $\delta^{34}S$. However, other samples show no correlation emerges between $\delta^{34}S$ and either Fe or Cd in this study. Some MVT deposits in the world found that Fe concentrations anticorrelated with $\delta^{34}S$ in banded sphalerite (Kuhlemann et al., 2001; Peevler et al., 2003; Gagnevin et al., 2014). In the Jinding deposit, sulfur isotope results in the same sample are in a narrow range. This correlation probably due to negative feedback effects and disequilibrium processes on BSR (Pfaff et al., 2011). We suggest that the sulfur activity to the element incorporation is likely affected less.

Therefore, this colloform sphalerite was likely formed by a high degree of supercooling, oversaturation, and rapid mixing between bacteriogenic sulfur and metal-rich in spaces of collapse dome (e.g., Roedder, 1968; Barrie et al., 2009; Pfaff et al., 2011; Gagnevin et al., 2012). As the changes in temperature, pH, and sulfur activity to pulses of hydrothermal fluids, isotope fractionation of sulfate-reducing organ and trace metals disequilibrium partitioning varied and resulted in significant variations in Fe and Cd at sphalerite growth zone. The incorporation of Fe-related elements and Cd-related elements are intertwined, with incorporation of trace elements and critical metals. These colloform sphalerite also existed in the world-class Irish-type and Mississippi Valley-type (MVT) deposits. These correlations remain statistically uncertain and warrant more in-depth analysis. Nevertheless, based on our observations, with fully consideration of potential exploration deposit of previous deposit, we suggested that these variability zones of layered

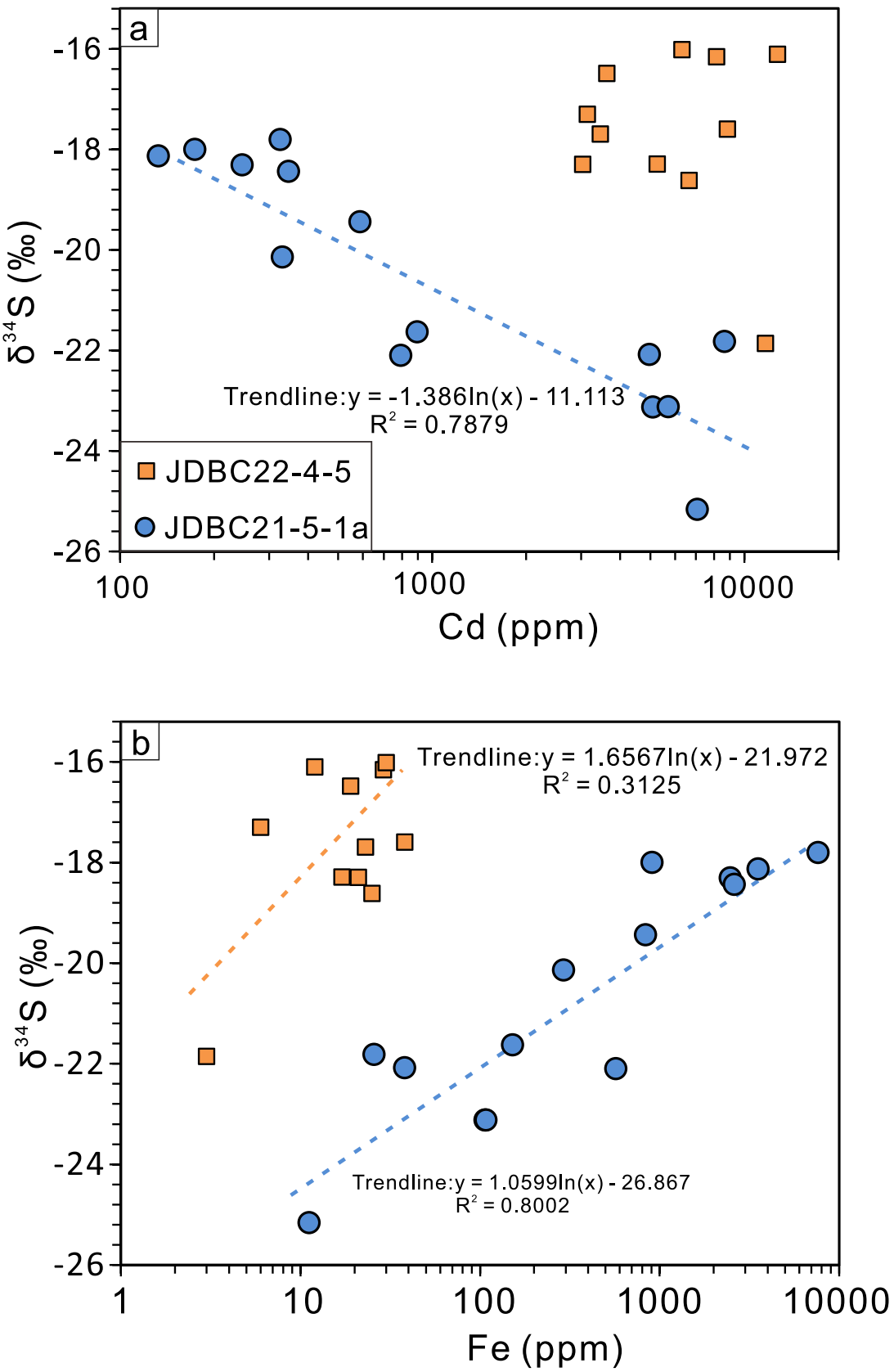

Fig. 16. Isotopic and chemical compositions of sphalerite. (a) plot of Cd concentration against S isotope and (b) plot of Fe concentration against S isotope.

sphalerite alternately enriched in Cd and Fe would likely provide useful insight for a potential economic Zn-Pb and associated critical metals mineral exploration deposit.

7. Conclusions

This detailed work carried out on the in-situ trace elements and sulfur isotopes of the layered sphalerite may provide important data and insights into the substitution mechanisms and the formation of the Jinding Zn-Pb deposit:

1. LA-ICP-MS analyses of trace elements reveal their coupled substitution mechanisms in sphalerite. Fe and Ge + Mn + Pb + As + Tl have a strong correlation, indicating their coupled substitution relation for element incorporation into sphalerite. The weak correlation between Cd and Cu + Ag + Sb suggests a possible role for a limited degree of Cu + Ag + Sb couple substitution, with the nano-scale inclusions. The presence of Fe and Cd assists incorporation of other components.

2. Trace element mappings show oscillatory zonation and color rhythmic banding at the scale of the micrometer in individual sphalerite layers. Highly variable color correlations in the Jinding sphalerite are attributed to the incorporation of minor elements. Brown sphalerite has high Fe, As, Mn, and Ge content, while Cd and Sb-rich sphalerite tend to be pale gray to colorless. The enriched Cd, as well as Sb, Ag, and Cu, in Jinding hydrothermal sphalerite and fluid inclusion results may suggest that the ore fluids may flow from metal-fertile sedimentary/basement sequences during their ascent.

3. In the Jinding hydrothermal system, the sulfur isotopic values show high isotope fractionation in the sphalerite from −28.4 to −0.5 ‰, suggesting a bacteriogenic sulfur origin. The sphalerite LA-ICP-MS data compared with the available S isotope record the fine-scale chemical variations that $\delta^{34}S$ is correlated with Fe and anti-correlated with Cd in limited samples.

4. Colloform sphalerite was likely formed by a high degree of supercooling, over-saturation, and rapid mixing between bacteriogenic sulfur and metal-rich in spaces of collapse dome. As the changes in temperature and pH, with less influence from sulfur activity, to pulses of hydrothermal fluids, Fe-related elements and Cd-related elements disequilibrium partitioning varied. These variability zones of sphalerite alternately enriched in Cd and Fe would likely indicate a potential environment for an economic Zn-Pb and associated critical metals mineral exploration deposit.

Funding

This research was financially supported by the National Science Foundation of China (42203070, 41830432) and the Project of Yunnan Provincial Science and Technology Department Basic Research Program (202301AT070014).

Declaration of Competing Interest

The authors declare that they have no known competing financial interests or personal relationships that could have appeared to influence the work reported in this paper.

Data availability

The data that has been used is confidential.

Acknowledgments

We thank Profs. Yan Tao and Jiafei Xiao for their help during fieldwork, and Zhihui Dai and Junjie Han for their assistance in trace element and sulfur isotope analysis. We are grateful to Prof. Zhixin Zhao and an anonymous reviewer for constructive reviews.

Appendix A. Supplementary data

Supplementary data to this article can be found online at https://doi.org/10.1016/j.oregeorev.2023.105794.

References

Anderson, G.M., 1973. The hydrothermal transport and deposition of galena and sphalerite near 100°C. Econ. Geol. 68, 80–492. https://doi.org/10.2113/gsecongeo.68.4.480.

Bao, Z.A., Chen, L., Zong, C.L., Yuan, H.L., Chen, K.Y., Dai, M.L., 2017. Development of pressed sulfide powder tablets for in situ sulfur and lead isotope measurement using LA-MC-ICP-MS. Int. J. Mass Spectrom. 421, 255–262. https://doi.org/10.1016/j.ijms.2017.07.015.

Barrie, C.D., Boyce, A.J., Boyle, A.P., Williams, P.J., Blake, K., Wilkinson, J.J., Lowther, M., McDermott, P., Prior, D.J., 2009. On the growth of colloform textures: A case study of sphalerite from the Galmoy orebody, Ireland. J. Geol. Soc. London 166, 563–582. https://doi.org/10.1144/0016-76492008-080.

Beaudoin, G., 2000. Acicular sphalerite enriched in Ag, Sb, and Cu embedded within colour banded sphalerite from the KokaneeM Range. BC. Can. Mineral 38, 1387–1398. https://doi.org/10.2113/gscanmin.38.6.1387.

Belissont, R., Boiron, M.C., Luais, B., Cathelineau, M., 2014. LA-ICP-MS analyses of minor and trace elements and bulk Ge isotopes in zoned Ge-rich sphalerites from the Noailhac-Saint-Salvy deposit (France): Insights into incorporation mechanisms and ore deposition processes. Geochim. Cosmochim. Acta 126, 518–540. https://doi.org/10.1016/j.gca.2013.10.052.

Bonnet, J., Mosser-Ruck, R., Caumon, M.C., Rouer, O., Andre-Mayer, A.S., Cauzid, J., Peifert, C., 2016. Trace element distribution (Cu, Ga, Ge, Cd and Fe) in sphalerite from the Tennessee MVT deposits, USA, by combined EMPA, LA-ICP-MS, Raman Spectroscopy and Crystallography. Can. Mineral 54, 1261–1284. https://doi.org/10.3749/canmin.1500104.

Chen, L., Yuan, H.L., Chen, K.Y., Bao, Z.A., Zhu, L.M., Liang, P., 2019. In situ sulfur isotope analysis by laser ablation MC-ICPMS and a case study of the Erlihe Zn-Pb ore deposit, Qinling orogenic belt, Central China. J. Asian Earth Sci. 176, 325–336. https://doi.org/10.1016/j.jseaes.2019.02.017.

Chi, G.X., Qing, H.R., Xue, C.J., Zeng, R., 2006. Modeling of fluid pressure evolution related to sediment loading and thrust faulting in the Lanping basin: Implications for the formation of the Jinding Zn-Pb deposit, Yunnan, China. J. Geochem. Explor. 89, 57–60. https://doi.org/10.1016/j.gexplo.2005.11.021.

Chi, G.X., Xue, C.J., Lai, J.Q., Qing, H.R., 2007. Sand injection and liquefaction structures in the Jinding Zn-Pb deposit, Yunnan, China: Indicators of an overpressured fluid system and implications for mineralization. Econ. Geol. 102, 739–743. https://doi.org/10.2113/gsecongeo.102.4.739.

Chi, G.X., Xue, C.J., Sun, X., Lai, J., Luo, P., Song, H., Li, S., Zeng, R., 2017. Formation of a giant Zn-Pb deposit from hot brines injecting into a shallow oil-gas reservoir in sandstones, Jinding, southwestern China. Terra Nova 29, 312–320. https://doi.org/10.1111/ter.12279.

Chung, S.L., Lee, T.Y., Lo, C.H., Wang, P.L., Chen, C.Y., Yem, N.T., Hoa, T.T., Wu, G.Y., 1997. Intraplate extension prior to continental extrusion along the Ailao Shan Red River shear zone. Geology 25, 311–314. https://doi.org/10.1130/0091-7613.

Chung, S.L., Lo, C.H., Lee, T.Y., Zhang, Y.Q., Xie, Y.W., Li, X.H., Wang, K.L., Wang, P.L., 1998. Diachronous uplift of the Tibetan Plateau starting 40 Myr ago. Nature 394, 769–773. https://doi.org/10.1038/29511.

Cook, N.J., Ciobanu, C.L., Pring, A., Skinner, W., Shimizu, M., Danyushevsky, L., Saini-Eidukat, B., Melcher, F., 2009. Trace and minor elements in sphalerite: a LA-ICPMS study. Geochim. Cosmochim. Acta 73, 4761–4791. https://doi.org/10.1016/j.gca.2009.05.045.

Cook, N.J., Etschmann, B., Ciobanu, C.L., Geraki, K., Howard, D.L., Williams, T., Rae, N., Pring, A., Chen, G., Johannessen, B., 2015. Distribution and substitution mechanism of Ge in a Ge-(Fe)-bearing sphalerite. Minerals 5, 117–132. https://doi.org/10.3390/min5020117.

Danyushevsky, L., Robinson, P., Gilbert, S., Norman, M., Large, R., McGoldrick, P., Shelley, M., 2011. Routine quantitative multi-element analysis of sulphide minerals by laser ablation ICP-MS: standard development and consideration of matrix effects. Geochem.: Explor. Environ., Anal. 11, 51–60. https://doi.org/10.1144/1467-7873/09-244.

Deng, J., Wang, Q.F., Li, G.J., Li, C.S., Wang, C.M., 2014a. Tethys tectonic evolution and its bearing on the distribution of important mineral deposits in the Sanjiang region, SW China. Gondw. Res. 26, 419–437. https://doi.org/10.1016/j.gr.2013.08.002.

Deng, J., Wang, Q.F., Li, G.J., Santosh, M., 2014b. Cenozoic tectonomagmatic and metallogenic processes in the Sanjiang region, southwestern China. Earth Sci. Rev. 138, 268–299. https://doi.org/10.1016/j.earscirev.2014.05.015.

Di Benedetto, F., 2005. Compositional zoning in sphalerite crystals. Am. Mineral. 90 (8–9), 1384–1392. https://doi.org/10.2138/am.2005.1754.

Frenzel, M., Hirsch, T., Gutzmer, J., 2016. Gallium, germanium, indium, and other trace and minor elements in sphalerite as a function of deposit type - a meta-analysis. Ore Geol. Rev. 76, 52–78. https://doi.org/10.1016/j.oregeorev.2015.12.017.

Frenzel, M., Voudouris, P., Cook, N.J., Ciobanu, C.L., Gilbert, S., Wade, B.P., 2021. Evolution of a hydrothermal ore-forming system recorded by sulfide mineral chemistry: a case study from the Plaka Pb-Zn-Ag Deposit, Lavrion, Greece. Mineral Deposita 57, 417–438. https://doi.org/10.1007/s00126-021-01067-y.

Gagnevin, D., Boyce, A.J., Barrie, C.D., Menuge, J.F., Blakeman, R.J., 2012. Zn, Fe and S isotope fractionation in a large hydrothermal system. Geochim. Cosmochim. Acta 88, 183–198. https://doi.org/10.1016/j.gca.2012.04.031.

Gagnevin, D., Menuge, J.F., Kronz, A., Barrie, C., Boyce, A.J., 2014. Minor elements in layered sphalerite as a record of fluid origin, mixing, and crystallization in the Navan Zn-Pb Ore Deposit, Ireland. Econ. Geol. 109, 1513–1528. https://doi.org/10.2113/econgeo.109.6.1513.

Gao, G.L., 1989. Review of geological origin about Jinding lead-zinc ore deposit. Earth Sci. 14, 467–475 in Chinese with English abs.

Gao, G.L., 1991. Formation age and involved problems on anhydrite ore in Jinding lead-zinc ore area. Yunnan Geol. 2, 191–206 in Chinese with English abs.

Gao, B.Y., Xue, C.J., Chi, G.X., Li, C., Qu, W.J., Du, A.D., Li, Z.H., Gu, H., 2012. Re-Os dating of bitumen in the giant Jinding Zn-Pb deposit, Yunnan and its geological significance. Acta Petrol. Sin. 28 (5), 1561–1567 in Chinese with English abs.

He, L., Song, Y., Chen, K., Hou, Z., Yu, F., Yang, Z., Wei, J., Li, Z., Liu, Y., 2009. Thrust-controlled, sediment-hosted, Himalayan Zn-Pb-Cu-Ag deposits in the Lanping foreland fold belt, eastern margin of Tibetan Plateau. Ore Geol. Rev. 36, 106–132. https://doi.org/10.1016/j.oregeorev.2008.11.001.

Hou, Z., Zaw, K., Pan, G., Mo, X., Xu, Q., Hu, Y., Li, X., 2007. Sanjiang Tethyan metallogenesis in S.W. China: Tectonic setting, metallogenic epochs and deposit types. Ore Geol. Rev. 31, 48–87. https://doi.org/10.1016/j.oregeorev.2004.12.007.

Hu, R., Turner, G., Burnard, P.G., Zhong, H., Ye, Z., Bi, X., 1998. Helium and argon isotopic geochemistry of Jinding superlarge Pb-Zn deposit. Sci. China Ser. D Earth Sci. 41, 442–448. https://doi.org/10.1007/BF02932698.

Huang, S.Q., Song, Y.C., Zhou, L.M., Leach, D., Chang, Z.S., Hou, Z.Q., 2021. Influence of organic matter on Re-Os dating of sulfides: insights from the giant Jinding sedimental-hosted Zn-Pb deposit, China. Econ. Geol. 117 (4), 737–745. https://doi.org/10.5382/econgeo.4881.

Jørgensen, B.B., 1979. A theoretical model of the stable sulfur isotope distribution in marine sediments. Geochim. Cosmochim. Acta 43, 363–374. https://doi.org/10.1016/0016-7037(79)90201-1.

Kuhlemann, J., Zeeh, S., 1995. Sphalerite stratigraphy and trace element composition of east Alpine Pb-Zn deposits (Drau Range, Austria-Slovenia). Econ. Geol. 90, 2073–2080. https://doi.org/10.2113/gsecongeo.90.7.2073.

Kuhlemann, J., Vennemann, T., Herlec, U., Zeeh, S., Bechstädt, T., 2001. Variations of sulfur isotopes, trace element compositions, and cathodoluminescence of Mississippi Valley-type Pb-Zn ores from the Drau Range, Eastern Alps (Slovenia-Austria): Implications for ore deposition on a regional versus microscale. Econ. Geol. 96, 1931–1941. https://doi.org/10.2113/gsecongeo.96.8.1931.

Kyle, J., Li, N., 2002. Jinding: A giant Tertiary sandstone-hosted Zn-Pb deposit, Yunnan, China. SEG Newsletter 50 (1), 9–16. https://doi.org/10.5382/SEGnews.2002-50.fea.

Leach, D.L., Sangster, D.F., Kelley, K.D., Large, R.R., Garven, G., Allen, C.R., Gutzmer, J., Walters, S., 2005. 100th anniversary special paper: Sediment-hosted lead-zinc deposits: A global perspective. Econ. Geol. 561–607.

Leach, D.L., Song, Y.C., Hou, Z.Q., 2017. The world-class Jinding Zn-Pb deposit: Ore formation in an evaporite dome, Lanping basin, Yunnan, China. Miner. Deposita 52, 281–296. https://doi.org/10.1007/s00126-016-0668-6.

Li, X.M., Tan, K.X., Gong, W.J., Gong, G.L., 2000. Study on the metallogenic epoch of the Jinding lead-zinc deposit with apatite fission track analysis. Geotecton. Metallog. 24, 282–286 in Chinese with English abs.

Liu, W.H., Mei, Y., Etschmann, B., Glenn, M., MacRae, C.M., Spinks, S.C., Ryan, C.G., Brugger, J., Paterson, D.J., 2023. Germanium speciation in experimental and natural sphalerite: Implications for critical metal enrichment in hydrothermal Zn-Pb ores. Geochim. Cosmochim. Acta 342, 198–214. https://doi.org/10.1016/j.gca.2022.11.031.

Liu, J.L., Wang, A.J., Cao, D.H., Xiu, Q.Y., 2004. Structure and evolution of the postcollisional fault structures in the Three River orogenic belt: Exemplified by the Cenozoic Jianchuan-Lanping basin. Geol. J. China Univ. 12, 488–499 in Chinese with English abs.

Liu, J.L., Tang, Y., Tian, M.D., Cao, S.Y., Zhao, L., Zhang, Z.C., Zhao, Z.D., Chen, W., 2012. The nature of the Ailao Shan-Red River (ASRR) shear zone: constraints from structural, microstructural and fabric analyses of metamorphic rocks from the Diancang Shan, Ailao Shan and Day Nui Con Voi massifs. J. Asian Earth Sci. 47, 231–251. https://doi.org/10.1016/j.jseaes.2011.10.020.

McLimans, R.K., Barnes, H.L., Ohmoto, H., 1980. Sphalerite stratigraphy of the upper Mississippi Valley zinc-lead district, southwest Wisconsin. Econ. Geol. 75, 351–361. https://doi.org/10.2113/gsecongeo.75.3.351.

Metcalfe, I., 2002. Permian tectonic framework and paleogeography of SE Asia. J. Asian Earth Sci. 20, 551–566. https://doi.org/10.1016/S1367-9120(02)00022-6.

Metcalfe, I., 2013. Gondwana dispersion and Asian accretion: Tectonic and palaeogeographic evolution of eastern Tethys. J. Asian Earth Sci. 66, 1–33.

Mo, X., Deng, J., Lu, F., 1994. Volcanism and the evolution of Tethys in Sanjiang area, southwestern China. J. SE Asian Earth Sci. 9, 325–333. https://doi.org/10.1016/0743-9547(94)90043-4.

Mu, L., Hu, R.Z., Bi, X.W., Tang, Y.Y., Lan, T.G., Lan, Q., Zhu, J.J., Peng, J.T., Oyebamiji., 2021. A new insights into the origin of the world-class Jinding Sediment-Hosted Zn-Pb Deposit, Southwestern China: evidence from LA-ICP-MS analysis of individual fluid inclusions. Econ. Geol. 116 (4), 883–907. https://doi.org/10.5382/econgeo.4826.

Pan, G.T., Xu, Q., Hou, Z.Q., Wang, L.Q., Du, D.X., Mo, X.X., Li, D.M., Wang, M.J., Li, X.Z., Jiang, X.S., 2003. The Ore-forming System of the Orogenic Processing in the Western "Sanjiang" Ploy-arc and the Resource Estimate. Geological Publishing House, Beijing, p. 420 in Chinese.

Paradis, S., Hannigan, P., and Dewing, K., 2007, Mississippi Valley-type lead-zinc deposits, in Goodfellow, W.D., ed., Mineral deposits of Canada: A synthesis of major deposit-types, district metallogeny, the evolution of geological provinces, and exploration methods. Geological Association of Canada, Mineral Deposits Division, Special Publication no. 5, 185–203.

Paton, C., Hellstrom, J., Paul, B., Woodhead, J., Hergt, J., 2011. Iolite: Freeware for the visualisation and processing of mass spectrometric data. J. Anal. At. Spectrom 26, 2508–2518. https://doi.org/10.1039/c1ja10172b.

Pattrick, R.A.D., Dorling, M., Polya, D.A., 1993. TEM study of indium bearing and copper-bearing growth-banded sphalerite. Can. Mineral. 31, 105–117.

Peevler, J., Fayek, M., Misra, K.C., Riciputi, L.R., 2003. Sulfur isotope microanalysis of sphalerite by SIMS: Constraints on the genesis of Mississippi Valley-type mineralization, from the Mascot-Jefferson City district, East Tennessee. J. Geochem. Explor. 80, 277–296. https://doi.org/10.1016/S0375-6742(03)00195-X.

Pfaff, K., Hildebrandt, L.H., Leach, D.L., Jacob, D.E., Markl, G., 2010. Formation of the Wiesloch Mississippi Valley-type Zn-Pb-Ag deposit in the extensional setting of the Upper Rhinegraben, SW Germany. Miner. Deposita 45, 647–666. https://doi.org/10.1007/s00126-010-0296-5.

Pfaff, K., Koenig, A., Wenzel, T., Ridley, I., Hildebrandt, L.H., Leach, D.L., Markl, G., 2011. Trace and minor element variations and sulfur isotopes in crystalline and colloform ZnS: Incorporation mechanisms and implications for their genesis. Chem. Geol. 286, 118–134. https://doi.org/10.1016/j.chemgeo.2011.04.018.

Pring, A., Wade, B., McFadden, A., Lenehan, C.E., Cook, N.J., 2020. Coupled substitutions of minor and trace elements in co-existing sphalerite and wurtzite. Minerals 10 (2), 147. https://doi.org/10.3390/min10020147.

Qin, G.J., Zhu, S.Q., 1991. Genetic model and ore prediction in Jinding Pb-Zn deposit: Yunnan. Geology 10 (2), 145–190 in Chinese with English abs.

Roedder, E., 1968. The non-colloidal origin of colloform textures in sphalerite ores. Econ. Geol. 63, 451–471. https://doi.org/10.2113/gsecongeo.63.5.451.

Shi, J.X., Yi, F.H., Wen, Q.C., 1983. The rock-ore characteristics and mineralization of Jinding lead-zinc deposit, Lanping. Yunnan Geol. 2 (3), 179–195 in Chinese with English abs.

Song, Y.C., Hou, Z.Q., Xue, C.D., Huang, S.Q., 2020. New mapping of the world-class Jinding Zn-Pb deposit, Lanping basin, southwest China: Genesis of ore host rocks and records of hydrocarbon-rock interaction. Econ. Geol. 115, 981–1002. https://doi.org/10.5382/econgeo.4721.

Spurlin, M.S., Yin, A., Horton, B.K., Zhou, J., Wang, J., 2005. Structural evolution of the Yushu-Nangqian region and its relationship to syncollisional igneous activity east-central Tibet. Geol. Soc. Am. Bull. 117, 1293–1317. https://doi.org/10.1130/B25572.1.

Tang, Y.Y., Bi, X.W., Fayek, M., Hu, R.Z., Wu, L.Y., Zou, Z.C., Feng, C.X., Wang, X.S., 2014. Microscale sulfur isotopic compositions of sulfide minerals from the Jinding Zn-Pb deposit, Yunnan Province, Southwest China. Gondw. Res. 26, 594–607. https://doi.org/10.1016/j.gr.2013.07.021.

Tao, X.F., Zhu, L.D., Liu, D.Z., Wang, G.Z., Li, Y.G., 2002. The Formation and Evolution of the Lanping Basin in Western Yunnan. J. Chengdu Univ. Technol. 29, 521–525 in Chinese with English abs.

Tapponnier, P., Lacassin, R., Leloup, P.H., Scharer, U., Zhong, D.L., Wu, H.W., Liu, X.H., Ji, S.C., Zhang, L.S., Zhong, J.Y., 1990. The Ailao Shan Red River metamorphic belt-Tertiary left-lateral shear between Indochina and South China. Nature 343, 431–437. https://doi.org/10.1038/343431a0.

Third Geological Team, 1984. The exploration report of the Jinding Zn-Pb deposit in Lanping County, Yunnan Province. Yunnan Bureau Geol. Mineral Resour. 50–106 in Chinese.

Wang, Q.F., Deng, J., Li, C.S., Li, G.J., Yu, L., Qiao, L., 2014. The boundary between the Simao and Yangtze blocks and their locations in Gondwana and Rodinia: constraints from detrital and inherited zircons. Gondw. Res. 26, 438–448. https://doi.org/10.1016/j.gr.2013.10.002.

Wang, J.H., Yin, A., Harrison, T.M., Grove, M., Zhang, Y.Q., Xie, G.H., 2001. A tectonic model for Cenozoic igneous activities in the eastern Indo-Asian collision zone. Earth Planet. Sci. Lett. 188, 123–133. https://doi.org/10.1016/S0012-821X(01)00315-6.

Wilson, S.A., Ridley, W.I., Koenig, A.E., 2002. Development of sulfide calibration standards for the laser ablation inductively coupled plasma mass spectrometry technique. J. Anal. Atomic Spectroscopy 17, 406–409. https://doi.org/10.1039/b108787h.

Xue, C.J., Zeng, R., Liu, S.W., Chi, G.X., Qing, H.R., Chen, Y.C., Yang, J.M., Wang, D.H., 2007. Geologic, fluid inclusion and isotopic characteristics of the Jinding Zn-Pb deposit, western Yunnan, South China: A review. Ore Geol. Rev. 31, 337–359. https://doi.org/10.1016/j.oregeorev.2005.04.007.

Xue, C.J., Chi, G.X., Fayek, M., 2015. Micro-textures and in situ sulfur isotopic analysis of spheroidal and zonal sulfides in the giant Jinding Zn-Pb deposit, Yunnan, China: Implications for biogenic processes. J. Asian Earth Sci. 103, 288–304. https://doi.org/10.1016/j.jseaes.2014.07.009.

Yalikun, Y., Xue, C., Symons, D.T.A., 2017. Paleomagnetic age and tectonic constraints on the genesis of the giant Jinding Zn-Pb deposit, Yunnan, China. Miner. Deposita 53, 1–15.

Yang, T.N., Ding, Y., Zhang, H.R., Fan, J.W., Liang, M.J., Wang, X.H., 2014. Two-phase subduction and subsequent collision defines the Paleotethyan tectonics of the southeastern Tibetan Plateau: Evidence from zircon U-Pb dating, geochemistry, and

structural geology of the Sanjiang orogenic belt, southwest China. Geol. Soc. Am. Bull. 126, 1654–1682. https://doi.org/10.1130/B30921.1.

Yardley, B.W.D., 2005. 100th anniversary special paper: Metal concentrations in crustal fluids and their relationship to ore formation. Econ. Geol. 100, 613–632. https://doi.org/10.2113/gsecongeo.100.4.613.

Ye, L., Cook, N.J., Ciobanu, C.L., Yuping, L., Qian, Z., Tiegeng, L., Wei, G., Yulong, Y., Danyushevskiy, L., 2011. Trace and minor elements in sphalerite from base metal deposits in South China: a LA-ICPMS study. Ore Geol. Rev. 39, 188–217. https://doi.org/10.1016/j.oregeorev.2011.03.001.

Yin, A., Harrison, T.M., 2000. Geologic evolution of the Himalayan Tibetan orogen. Annu. Rev. Earth Planet. Sci. 28, 211–280. https://doi.org/10.1146/annurev.earth.28.1.211.

Yunnan Bureau Geological Mineral Resource, 1990. Regional geology of Yunnan Province. Geology Publishing House, Beijing, p. 729 in Chinese.

Zhang, B., Zhang, J., Zhong, D., 2010. Structure, kinematics and ages of transpression during strain-partitioning in the Chongshan shear zone, western Yunnan, China. J. Struct. Geol. 32, 445–463. https://doi.org/10.1016/j.jsg.2010.02.001.